International Journal of Mechanical Sciences 262 (2024) 108731

Contents lists available at ScienceDirect

International Journal of Mechanical Sciences

journal homepage: www.elsevier.com/locate/ijmecsci

Nonlinear dynamics of a compact and multistable mechanical energy harvester

Luã G. Costa, Marcelo A. Savi *

Universidade Federal do Rio de Janeiro, COPPE - Mechanical Engineering Center for Nonlinear Mechanics, 21941-914 Rio de Janeiro RJ, Brazil

ARTICLE INFO

Keywords:
Energy harvesting
Smart materials
Nonlinear dynamics
Chaos
Lyapunov exponents
Compact structures
Multistability
Multiple DoF structures

ABSTRACT

The use of smart materials as transducers in mechanical energy harvesting systems has gained significant attention in recent years. Despite the numerous proposed solutions in the literature, challenges still exist in terms of their implementation within limited spaces while maintaining optimal performance. This paper addresses these challenges through the concepts of compactness and space-efficient design, as well as the incorporation of nonlinear characteristics and additional degrees-of-freedom. A multistable dual beam nonlinear structure featuring two magnetic interactions and two piezoelectric transducers is presented. A reduced order model with 2-degrees-of-freedom is established based on the harvester structure in order to capture the essential qualitative characteristics of the system. Stability analysis demonstrates that the combination of two nonlinear magnetic interactions furnish unprecedented multistable characteristics to this type of harvester. A framework using a nonlinear dynamics perspective is established to analyze multistable systems based on energy harvesting purposes. Different dynamical and stability characteristics are determined by the differences in the system stiffness ratio. Parametric analyses are carried out classifying regions of high performance in the external excitation parameter space. These regions are associated with rich and complex dynamics. Finally, a comprehensive comparison is conducted between the proposed harvester and the classical bistable harvester, revealing improvements in performance across nearly all relevant conditions. These findings highlight the enhanced capabilities of the proposed harvester design, solidifying its potential of application in diverse energy harvesting scenarios.

1. Introduction

The rapid development of society in recent years have caused an increase of global energy demand. Induced by modern science tools and elements of Industry 4.0, such as wireless electronic devices and smart systems, energetic issues are related to bottlenecks that need to be overcome. Besides, the need of environmental-friendly power supplies due to climate changes and the reduction of e-waste [1,2] are motivating the development of new paradigms. This scenario results in the need for new strategies and creative solutions that can be viable in long-term applications. In this regard, the constant evolution of semiconductor technology keeps significantly reducing the power consumption of electronic systems in general, especially wireless devices [3]. This is making the harvesting of environmental wasted energy as vibration, sound, wind, sea waves and biomechanical motion attractive as an alternative power supply to traditional batteries [4] and small-medium size systems, as these sources of mechanical energy can be enough to power from small electronic devices to small scale centers [5].

To harvest the available environment mechanical energy, transducer mechanisms as electromagnetic converters, triboelectric structures and smart materials can be cited as the most common in the literature [6,7]. Concerning smart materials, piezoelectric is the most common type [8], but magnetostrictive [9,10], flexoelectric [11,12] and magnetic shape memory alloys [13,14] also appear in the literature. These transducers can be attached to a host structure that serves as an energy bridge between the environment and the transducer. Each of these transducers have distinct unique advantages and disadvantages. For example, many techniques to produce synthetic piezoelectric materials with high coupling coefficients and in different shapes have already been mastered resulting in an easy procedure for energy harvesting purposes. In this regard, it should be pointed out the spring energy harvester developed in the works of Kim et al. [15] and Kim et al. [16]. Magnetostrictive materials can also have high coupling coefficients and present no depolarization/aging problems, however can be difficult to integrate with microelectronic devices due to the need of bulk pickup coils. For a more complete comparison

* Corresponding author.
E-mail address: savi@mecanica.ufrj.br (M.A. Savi).

https://doi.org/10.1016/j.ijmecsci.2023.108731
Received 4 May 2023; Received in revised form 28 August 2023; Accepted 3 September 2023
Available online 16 September 2023

among energy harvesting transducers refer to Wang and Yuan [17] and Vallem et al. [18].

Despite the transducer mechanism, the structure itself exerts a major influence on the performance of the energy harvester. The choice for a proper structural design configuration is an essential point. The archetypal of the energy harvesting structure is based on the cantilever beam design [19]. Many efforts have been done to fully model and experimentally validate this type of design, making the cantilever arrangement one of the most common designs found in the literature [20–22]. The great significant shortcoming of this design is the lack of efficiency when operating at frequencies that deviate significantly from its natural frequency. Under these conditions, the harvester deflection tends to decrease, resulting in a low electrical output and limiting its application [23]. This drawback leads researchers to insert mechanical modulations in this design to enhance its performance.

The evolution of the cantilever design has led to the incorporation of additional mechanical degrees-of-freedom (DoF) to operate in the parallel direction of the external input excitation, creating an additional efficient operating region [24]. This progression led to the design proposed by Wu et al. [25], which comprises of an outer beam and an inner beam. This configuration brings the first two natural frequencies closer together, thereby creating an larger operating region for the harvester and rendering the 2-DoF cantilever-based system more compact in nature.

The improvement of the cantilever system has also led to the incorporation of nonlinear characteristics. A variety of nonlinear modulations have been proposed, and new ones continue to be proposed to this day [26,27]. In this regard, nonlinear energy harvesters have been found to be highly effective in delivering broadband performance, making them well-suited for general applications. Multistable energy harvesters, as the name suggests, belong to a class of systems that exhibit multiple stable positions. This approach has proven to be effective as it increases the deflection of the system, enhancing its energy harvesting capabilities. Various techniques can be employed to achieve multistability, such as incorporating magnetic interactions [28] or inducing the mechanical buckling by axial forces [29] or magnetic induced buckling [30] . As far as this is concerned, researchers have extensively studied the potential of multistability in one-degree-of-freedom systems, exploring different configurations including bistable [31,32], tristable [33,34], tetrastable [35,36], and pentastable [37,38] systems. The problem of adding more stable positions is the creation of a potential energy barrier, which can reduce its performance depending on the level of the input excitation. Generally, the literature shows that increasing the number of stable positions can reduce this barrier.

The construction of multistable harvesters involves various aspects, such as the position and angle of the magnets, as well as potential asymmetries, which are crucial considerations. Kumar et al. [39] revealed the potential benefits of employing a monostable asymmetric nonlinear system in specific cases, surpassing the symmetric bistable system. Wang et al. [40] demonstrated that the utilization of an asymmetric bistable potential negatively impacts energy harvesting capacity when the system dynamics originate from the vicinity of the deeper equilibrium point. However, if an initial condition is established near the shallower energy well, performance can be improved. Cao et al. [41] established that modifying the angle of the magnets responsible for inducing bistability can significantly alter the dynamics of the classical bistable energy harvester. Furthermore, Norenberg et al. [42] demonstrated that adjusting the slope angles of magnets can effectively counteract the adverse effects of a bistable asymmetric potential.

Another strategy is to exploit non-smoothness, for example, incorporating impacts into the system. This idea increases the system bandwidth, but at the cost of reducing its maximum output power [43]. This approach is well-suited for scenarios where the ambient mechanical excitation exhibits a wide range of frequencies. The disadvantage is that the non-smoothness can cause mechanical wear over time, leading to structural damage in long-term applications [44].

New ideas for nonlinear modulations are still being developed. The synergistic use of smart materials is one possibility and two interesting designs make use of shape memory materials to achieve adaptability in energy harvesting systems. Adeodato et al. [45] employed a Nitinol Shape memory alloy (SMA) spring attached to the free end of the cantilever beam to alter the natural frequency of the energy harvesting system by controlling the temperature. Yuan et al. [46] proposed a strategy of using a light-activated shape memory polymer (LASMP) layer attached to the cantilever beam to control the natural frequency of the structure. In this case, the Young modulus of the LASMP can be adjusted according to the level of light exposure. Finally, a quasi-zero-stiffness energy harvester was presented by Margielewicz et al. [47], which is characterized by an almost flat potential energy function, countering the drawbacks of multistable classical systems. However, the disadvantage of this method is that the quasi-zero module is composed of three springs attached to the free end of the cantilever beam, making it difficult to set up and potentially not a compact solution.

Novel designs have also been presented in the literature. Caetano and Savi [48] proposed a pizza-shaped system exploiting multiple degrees-of-freedom and obtaining a broadband device, where it was concluded that irregular structures showed to be the most effective to enhance energy harvesting capacity. Afterward, Caetano and Savi [49] proposed a star-shaped device coupled with inertial pendulum-like masses that provides either broadband characteristics and multidirectionality. Yang et al. [50] suggested an enhancement to the cantilever design by incorporating an arc-shaped segment that significantly improved its performance, and Zhou et al. [51] developed a distributed parameter model of this new harvester. Subsequent works studied the incorporation of various types multistability characteristics in this type of structure with static [52–54] and variable potential aspects [55]. Additionally, Wu et al. [56] presented a piezoelectric spring-pendulum architecture based on a binder clip structure capable of effectively scavenging ultra-low frequency and multidirectional vibration energies. Nonlinear frequency-up conversion mechanisms [57,58] showed to be capable to convert a low frequency external excitation motion into a higher frequency response. In addition, other interesting subjects related to mechanical energy harvesting are associated with nonlinear rotational harvesters [59], metastructures with both vibration suppression and energy harvesting characteristics [60], and vortex-induced energy harvesting [61–63].

The design feasibility is restricted as many of the mechanical energy harvester applications dispose of limited available space. The search for compact and efficient solutions remains a challenge. To address this, Wu et al. [64] successfully combined the magnetically induced bistable concept with a dual beam compact structure they had previously designed in Wu et al. [25] to create a bistable dual beam energy harvester with a compact design and good performance. Subsequently, Upadrashta and Yang [65] and Krishnasamy et al. [66] conducted finite element simulations and experiments to validate and formalize a distributed parameter modeling of this design.

Inspired by classical bistable energy harvester and bistable dual-beam structures, and motivated by the trend of maximizing energy harvesting capabilities through compact designs, this work proposes a new nonlinear dual beam structure with two sets of magnets and transducers. Compared with the existing literature, the novelty of this harvester relies on the addition of a second set of magnets and the insertion of an additional transducer. This design enables efficient utilization of previously unused space and results in unprecedented multistable characteristics, enhancing the overall functionality of this type of harvester.

An analysis framework is established using a nonlinear dynamics perspective, aiming to standardize the analysis of multistable energy harvesting systems by the usage of suitable tools. The first stage is related to Section 2, where a reduced-order 2-DoF Duffing-type system is modeled to represent the main qualitative aspects of the system's dynamics. A normalization of the model is done in order to generalize

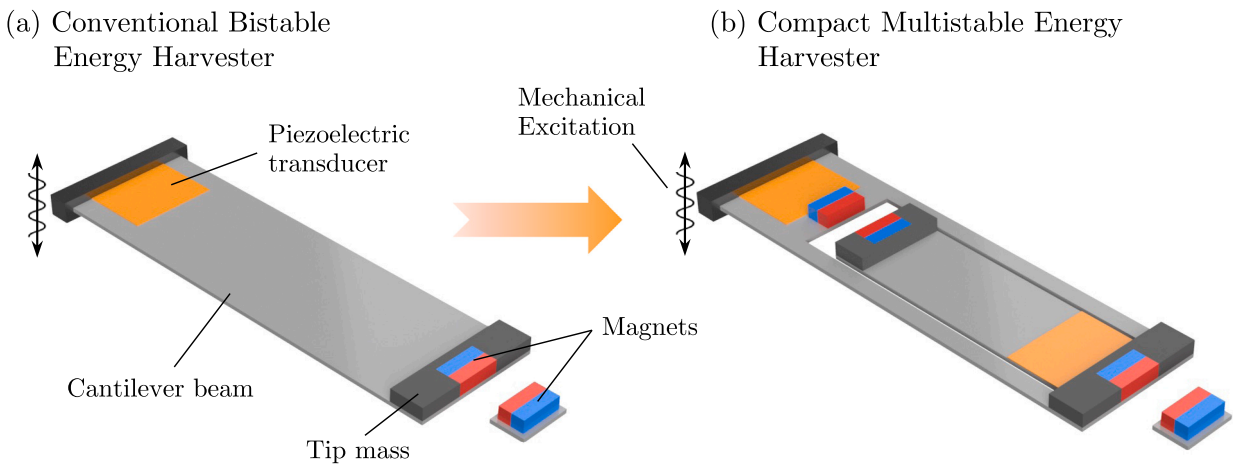

Fig. 1. Conceptual representation of the novel energy harvester, illustrating its compact and space-efficient design, which is comparable in size to the traditional bistable energy harvester.

the analysis, and suitable performance metrics are established. The second stage, detailed in Section 3, performs a stability investigation using linear stability theory, the potential energy function and basins of attraction to analyze the equilibrium states and their evolution through the variation of key parameters. In Section 4, the third and fourth stages are conducted, where parametric investigations are employed to evaluate the best configurations and operational conditions of the system based on energy harvesting capacity. The third stage consists in the usage of standard nonlinear dynamics tools as Poincaré maps and Lyapunov exponents to characterize the system dynamics, identifying the predominant dynamical attractors and how they influence the system's performance. In addition, the connection between dynamics and performance is accomplished, showing that rich and complex dynamics can be associated with enhanced performance. The fourth stage establishes suitable metrics for the comparison of the proposed system with the classical bistable energy harvester. The best operational conditions are discussed. In general, this framework provides an objective and comprehensive evaluation of multistable systems, facilitating its development and implementation.

2. Design concept and theoretical model

This section is devoted to exploring the design concept of the novel multistable compact energy harvester, as well as detailing the underlying assumptions employed for its modeling.

A energy harvesting system design based on the classical cantilever beam structure characteristics is proposed, increasing the number of degrees-of-freedom and employing nonlinear modulation based on magnetic interactions. This idea combines previously validated concepts of the literature, achieving compactness and performance by fully utilizing all available high strain rate space.

This goal is accomplished building a classical bistable energy harvester but introducing new relevant degrees-of-freedom by cutting off the main beam, as done by Wu et al. [25,64], Zhao et al. [67] and Bouhedma et al. [68]. Additionally, a new set of magnetic interactions and an extra piezoelectric transducer are integrated into the new inner beam. Fig. 1 presents the conceptual design of the novel device compared with the classical bistable cantilever beam. This novel design offers a more efficient use of space and potentially greater performance capabilities compared with the classical version.

2.1. Physical modeling

The proposed energy harvester is modeled by considering a 2-DoF multistable device assuming the first vibration mode as reference, as shown in Fig. 2. This prototype represents the main characteristics of the energy harvester, presenting 1-DoF for each beam. Therefore, by considering that subscript $i = 1, 2$ denotes the properties associated with each one of the two degrees-of-freedom, m_i represents the mass, k_i is the equivalent structural stiffness and c_i is the equivalent dissipation coefficient. Additionally, piezoelectric patches are attached to the structure and can be represented by the electromechanical coupling coefficient, θ_i, an internal capacitance C_{pi}, and an internal resistance, R_{pi}.

The electrical circuits are assumed to be simple resistive circuits that are connected to the piezoelectric elements, each with a load resistance, R_{li}. The output voltage of each circuit is represented by $v_i(t)$, and the equivalent electrical resistance, R_i, of each circuit is composed by the piezoelectric internal resistance and the load resistance connected in parallel, such that $R_i = R_{li}R_{pi}/\left(R_{li} + R_{pi}\right)$.

The system is subjected to a base excitation of $z_b = A\sin\omega t$, where A and ω represent the excitation amplitude and frequency, respectively. Furthermore, the displacement of each mass is represented by $z_i(t)$ and the respective positive directions related to the real harvester's structure are presented in Fig. 2c, that is, when $z_1(t)$ is positive, the motion of the outer beam is directed upward, whereas when $z_2(t)$ is positive, the motion of the inner beam presents an downward direction [66]. Also, the upper dot represents derivatives with respect to time, as $\dot{\square} = d\square/dt$, and the effects of gravity are neglected.

The Euler–Lagrange equations are defined from 2 mechanical coordinates (z_1, z_2) and 2 electrical coordinates ($\psi_1(t)$, $\psi_2(t)$), the magnetic flux linkages. Therefore, it is assumed that $\mathbf{u} = [z_1(t), z_2(t), \psi_1(t), \psi_2(t)]$, resulting in the following equation,

$$\frac{d}{dt}\left(\frac{\partial \mathcal{L}}{\partial \dot{u}_i}\right) - \frac{\partial \mathcal{L}}{\partial u_i} + \frac{\partial D}{\partial \dot{u}_i} = 0, \tag{1}$$

where the Lagrangian, $\mathcal{L} = T - U + W_e^*$, is given by the sum of the kinetic energy, T, the potential energy, U, and the total piezoelectric coenergy, W_e^*. Moreover, the total energy dissipation is defined from the function D.

By assuming that magnetic interactions can be reasonably approximated by polynomial Duffing-type restitution forces, associated with cubic nonlinearity of the form $f_i(z_i) = a_i z_i(t) + b_i z_i(t)^3$ [69,70], the potential energy is written as in Eq. (2), while kinetic energy is defined as in Eq. (3).

$$U = \frac{1}{2}\left(a_1 + k_1\right) z_1(t)^2 + \frac{1}{4}b_1 z_1(t)^4 + \frac{1}{2}k_2\left[z_2(t) - z_1(t)\right]^2 + \frac{1}{2}a_2 z_2(t)^2 + \frac{1}{4}b_2 z_2(t)^4, \tag{2}$$

$$T = \sum_{i=1}^{2}\frac{1}{2}m_i\left[\dot{z}_i(t) + \dot{z}_b(t)\right]^2, \tag{3}$$

where a_i and b_i are the Duffing coefficients that represent the effect of the magnetic interactions that can be estimated by a polynomial fitting to experimental data [71].

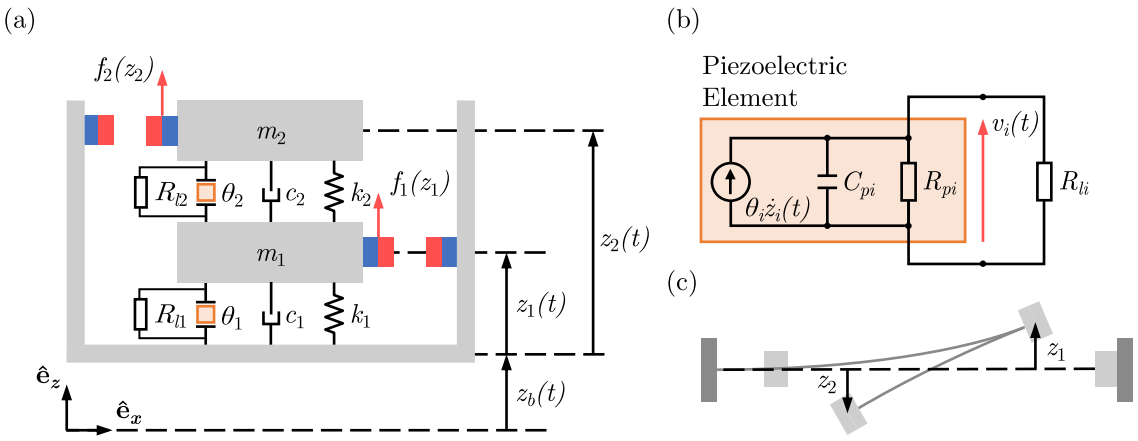

Fig. 2. Lumped model representing (a) the compact multistable energy harvester structure, (b) the equivalent electrical circuit composed by the piezoelectric element attached to a resistance, and (c) the respective positive z_i directions for each DoF of the reduced order model related to the beam's structure.

The piezoelectric effect is considered by the definition of the total piezoelectric coenergy, W_e^*, as showed by Preumont [72], where the flux linkages are such that $\psi_1(t) = v_1(t)$ and $\psi_2(t) = v_2(t)$. Therefore:

$$W_e^* = \sum_{i=1}^{2} \left[\frac{1}{2} C_{p_i} \psi_i(t)^2 \right] + \theta_1 \psi_1(t) z_1(t) + \theta_2 \psi_2(t) \left[z_2(t) - z_1(t) \right]. \tag{4}$$

The total energy dissipation can be described by the sum of the Rayleigh's dissipation function [73] and the electrical dissipation function as follows

$$D = \frac{1}{2} c_1 \dot{z}_1(t)^2 + \frac{1}{2} c_2 \left[\dot{z}_2(t) - \dot{z}_1(t) \right]^2 + \sum_{i=1}^{2} \left[\frac{\dot{\psi}_i(t)^2}{2R_i} \right]. \tag{5}$$

A normalization approach is carried out by considering a reference length L and a reference voltage V, resulting in the dimensionless electromechanical equations given by Eqs. (6) to (9), where the term (τ) that indicates normalized time dependency are conveniently suppressed.[1]

$$\ddot{\bar{z}}_1 + 2\zeta_1 \dot{\bar{z}}_1 - 2\zeta_2 \left(\dot{\bar{z}}_2 - \dot{\bar{z}}_1 \right) + \left(1 + \alpha_1 \right) \bar{z}_1 + \beta_1 \bar{z}_1^3 - \rho \Omega_s^2 \left(\bar{z}_2 - \bar{z}_1 \right) - \chi_1 \bar{v}_1 + \chi_2 \bar{v}_2 = -\ddot{\bar{z}}_b; \tag{6}$$

$$\rho \ddot{\bar{z}}_2 + 2\zeta_2 \left(\dot{\bar{z}}_2 - \dot{\bar{z}}_1 \right) + \alpha_2 \bar{z}_2 + \beta_2 \bar{z}_2^3 + \rho \Omega_s^2 \left(\bar{z}_2 - \bar{z}_1 \right) - \chi_2 \bar{v}_2 = -\ddot{\bar{z}}_b; \tag{7}$$

$$\dot{\bar{v}}_1 + \varphi_1 \bar{v}_1 + \kappa_1 \dot{\bar{z}}_1 = 0; \tag{8}$$

$$\dot{\bar{v}}_2 + \varphi_2 \bar{v}_2 + \kappa_2 \left(\dot{\bar{z}}_2 - \dot{\bar{z}}_1 \right) = 0. \tag{9}$$

The electromechanical system can be rewritten in its canonical form, $\dot{\bar{\mathbf{q}}} = \mathbf{f}(\bar{\mathbf{q}})$ with $\bar{\mathbf{q}} = [\bar{z}_1, \dot{\bar{z}}_1, \bar{z}_2, \dot{\bar{z}}_2, \bar{v}_1, \bar{v}_2]$ and dimensionless parameters related to equations of motion are presented in Table 1. Also, a proper comprehension of the system behavior needs to consider the normalized form of the potential energy, expressed in Eq. (10).

$$\bar{U} = \frac{1}{2} \left(1 + \alpha_1 \right) \bar{z}_1^2 + \frac{1}{4} \beta_1 \bar{z}_1^4 + \frac{1}{2} \rho \Omega_s^2 \left(\bar{z}_2 - \bar{z}_1 \right)^2 + \frac{1}{2} \alpha_2 \bar{z}_2^2 + \frac{1}{4} \beta_2 \bar{z}_2^4. \tag{10}$$

2.2. Performance metrics

The performance analysis of the energy harvester device is usually defined by the electrical output variables. In this regard, either instantaneous or average values can be monitored. The instantaneous electrical power in a simple resistive circuit is commonly represented by Eq. (11). The average electrical power is represented by Eq. (12), where v_i^{RMS} are the root mean square of the output voltages.

$$P_i = \frac{1}{R_i} v_i^2, \tag{11}$$

$$P_{\mathrm{avg}} = \sum_{i=1}^{2} \left[\frac{1}{t_f - t_0} \int_{t_0}^{t_f} P_i \, dt \right] = \sum_{i=1}^{2} \left[\frac{1}{R_i} \left(v_i^{\mathrm{RMS}} \right)^2 \right]. \tag{12}$$

Furthermore, an average power density can be calculated by dividing the average power by the number of degrees-of-freedom of the system (n_{DoF}), resulting in Eq. (13).

$$P_{\mathrm{avg}}^{\mathrm{den}} = \frac{P_{\mathrm{avg}}}{n_{\mathrm{DoF}}}. \tag{13}$$

Based on these concepts and according to Table 1, the normalized average electrical output power and the normalized average electrical output power density can be determined by Eqs. (14) and (15), respectively.

$$\bar{P}_{\mathrm{avg}} = \sum_{i=1}^{2} \left[\frac{1}{\tau_f - \tau_0} \int_{\tau_0}^{\tau_f} \bar{P}_i \, d\tau \right] = \sum_{i=1}^{2} \left[\varphi_i \left(\bar{v}_i^{\mathrm{RMS}} \right)^2 \right], \tag{14}$$

$$\bar{P}_{\mathrm{avg}}^{\mathrm{den}} = \frac{\bar{P}_{\mathrm{avg}}}{n_{\mathrm{DoF}}}. \tag{15}$$

3. Stability analysis

The multistability of the system has shown to be an interesting point to be investigated since it is directly related to the enhancement of the energy harvesting capacity. This section dedicates a special attention to this issue. The equilibrium configurations of the system can be determined by identifying $\dot{\bar{\mathbf{q}}} = \mathbf{f}(\bar{\mathbf{q}}) = \mathbf{0}$. The nature of each equilibrium point can be determined through a linearization around each point, evaluating the Jacobian matrix, $\mathbf{J}$, displayed in Eq. (16).

$$\mathbf{J} = \nabla^{\mathrm{T}} \mathbf{f}(\bar{\mathbf{q}}) = \begin{bmatrix} 0 & 1 & 0 & 0 & 0 & 0 \\ -1 - \alpha_1 - \rho\Omega_s^2 - 3\beta_1 \bar{z}_1^2 & -2\left(\zeta_1 + \zeta_2\right) & \rho\Omega_s^2 & 2\zeta_2 & \chi_1 & -\chi_2 \\ 0 & 0 & 0 & 1 & 0 & 0 \\ \Omega_s^2 & \dfrac{2\zeta_2}{\rho} & -\dfrac{\alpha_2 + \rho\Omega_s^2 + 3\beta_2 \bar{z}_2^2}{\rho} & -\dfrac{2\zeta_2}{\rho} & 0 & \dfrac{\chi_2}{\rho} \\ 0 & -\kappa_1 & 0 & 0 & -\varphi_1 & 0 \\ 0 & \kappa_2 & 0 & -\kappa_2 & 0 & -\varphi_2 \end{bmatrix}. \tag{16}$$

The stability characteristics of each point is evaluated from the eigenvalues of the Jacobian matrix, μ_j $(j = 1, \ldots, 6)$. These points can be classified into three sets:

1. Stable if $\left\{ \mu_j \in \mathbb{C} \mid Re\left(\mu_j\right) < 0 \right\}$;
2. Unstable if $\left\{ \mu_j \in \mathbb{C} \mid Re\left(\mu_j\right) > 0 \right\}$;
3. Center if $\left\{ \mu_j \in \mathbb{C} \mid Re\left(\mu_j\right) = 0 \right\}$.

[1] Note that upper dots in the normalized case are related to the derivatives with respect to the normalized time, as $\dot{\square} = d\square/d\tau$.

Table 1
System parameters and values used in the analyses.

Parameter description	Symbol	Definition	Value
Linearized natural frequency of the 1st mass	ω_1	$\sqrt{k_1/m_1}$	–
Linearized natural frequency of the 2nd mass	ω_2	$\sqrt{k_2/m_2}$	–
Normalized time	τ	$\omega_1 t$	–
Normalized displacement of the 1st mass	$\bar{z}_1(\tau)$	$z_1(t)/L$	–
Normalized displacement of the 2nd mass	$\bar{z}_2(\tau)$	$z_2(t)/L$	–
Normalized voltage of the 1st circuit	$\bar{v}_1(\tau)$	$v_1(t)/V$	–
Normalized voltage of the 2nd circuit	$\bar{v}_2(\tau)$	$v_2(t)/V$	–
Normalized base excitation frequency	Ω	ω/ω_1	$0.01 \rightarrow 10$
Normalized base excitation amplitude	γ	A/L	$0.01 \rightarrow 2$
Normalized base excitation displacement	$\bar{z}_b(\tau)$	$\gamma \sin(\Omega\tau)$	–
Ratio of masses	ρ	m_2/m_1	$0.5 \rightarrow 1.5$
Normalized mechanical damping coefficient of the 1st mechanical DoF	ζ_1	$c_1/(2\omega_1 m_1)$	0.025
Normalized mechanical damping coefficient of the 2nd mechanical DoF	ζ_2	$c_2/(2\omega_1 m_1)$	0.025
Ratio of linearized natural frequencies	Ω_s	ω_2/ω_1	$0.25 \rightarrow 2.0$
Normalized linear restitution coefficient of the 1st mechanical DoF	α_1	$a_1/(\omega_1^2 m_1)$	-2
Normalized linear restitution coefficient of the 2nd mechanical DoF	α_2	$a_2/(\omega_1^2 m_1)$	-1
Normalized nonlinear restitution coefficient of the 1st mechanical DoF	β_1	$b_1 L^2/(\omega_1^2 m_1)$	1
Normalized nonlinear restitution coefficient of the 2nd mechanical DoF	β_2	$b_2 L^2/(\omega_1^2 m_1)$	1
Normalized 1st piezoelectric coupling coefficient in the mechanical ODE	χ_1	$\theta_1 V/(k_1 L)$	0.05
Normalized 2nd piezoelectric coupling coefficient in the mechanical ODE	χ_2	$\theta_2 V/(k_1 L)$	0.05
Normalized 1st piezoelectric coupling coefficient in the electrical ODE	κ_1	$\theta_1 L/(C_{p1} V)$	0.5
Normalized 2nd piezoelectric coupling coefficient in the electrical ODE	κ_2	$\theta_2 L/(C_{p2} V)$	0.5
Normalized electrical resistance of the 1st circuit	φ_1	$1/(C_{p1} R_1 \omega_1)$	0.05
Normalized electrical resistance of the 2nd circuit	φ_2	$1/(C_{p2} R_2 \omega_1)$	0.05
Normalized electrical output power of the 1st electrical DoF	$\bar{P}_1(\tau)$	$P_1(t)/(C_{p1}\omega_1 V^2)$	–
Normalized electrical output power of the 2nd electrical DoF	$\bar{P}_2(\tau)$	$P_2(t)/(C_{p2}\omega_1 V^2)$	–

Besides that, the stability of the linearized system at the vicinity of an equilibrium point corresponds to the nonlinear system as long as the point is hyperbolic, meaning that there is not an eigenvalue that vanishes the real part $\left(Re\left(\mu_j\right) \neq 0, \forall j\right)$ [74].

On this basis, all solutions are hyperbolic and the unstable points can be split into two distinct groups: saddle-type unstable points and source-type unstable points. Saddle-type unstable points exhibit one positive eigenvalue, indicating the presence of a single unstable direction. On the other hand, source-type unstable points exhibit two positive eigenvalues, indicating the presence of two unstable directions. Additionally, the stability analysis can be further complemented by evaluating the normalized form of the potential energy function, as detailed in Eq. (10), and by constructing the basins of attraction of the non-forced system. This provides a comprehensive understanding of the system's stability characteristics.

The solution of the problem $\dot{\bar{\mathbf{q}}} = \mathbf{f}(\bar{\mathbf{q}}) = \mathbf{0}$ defines equilibrium positions that is a collection of sets of the form $\left\{\bar{z}_1, \dot{\bar{z}}_1, \bar{z}_2, \dot{\bar{z}}_2, \bar{v}_1, \bar{v}_2\right\} = \left\{\bar{Z}_1, 0, \bar{Z}_2, 0, 0, 0\right\}$. The stability analysis allows a visualization through the subset $\left\{\bar{z}_1, \bar{z}_2\right\} = \left\{\bar{Z}_1, \bar{Z}_2\right\}$. Fig. 3 illustrates the stability for different values of Ω_s, with a fixed mass ratio of $\rho = 1$. The colorbar represents the potential energy levels, with darker colors representing lower energies and lighter colors representing higher energies. Fig. 4 presents the basins of attraction for different Ω_s using four colors to indicate attractors, which are the stable equilibrium points (SEP_i, $i = 1, \ldots, 4$) where the system converges to if released from initial conditions within -2 to 2 for each displacement $\bar{z}_1$ and $\bar{z}_2$. In both Figures, blue dots indicate stable equilibria, orange triangles indicate unstable saddle-type equilibria, and red polygons indicate unstable source-type equilibria.

It is noticeable that for $\Omega_s < 0.6$, the system exhibits 9 equilibrium positions, 4 of which are stable, 4 are unstable saddle-type, and 1 is unstable source-type. The increase of Ω_s results in a reduction of the distances between SEP_3, SEP_4, and the saddle-type points in their vicinity, which elevates the potential energy level of the local minima and decreases the likelihood of the system being attracted towards SEP_3 and SEP_4. When Ω_s reaches a value between 0.55 and 0.6, SEP_3 and SEP_4 disappears, becoming new saddle-type unstable points. This behavior defines 5 equilibrium points, with 2 stable, 2 saddle-type unstable, and 1 source-type unstable. Further, 2 of 3 unstable positions disappear between $0.6 < \Omega_s < 0.75$, resulting in a system with 3 equilibrium positions, of which 2 are stable and 1 is saddle-type unstable. The configuration remains the same for $\Omega_s > 0.75$ and the potential energy surface becomes thinner as Ω_s increases.

The impact of the mass ratio, ρ, on the stability of the system is analyzed in Figs. 5 and 6, where Ω_s is kept constant at 0.5. Results show that the increase of ρ results in a slower reduction of the number of equilibrium points. This can be attributed to the term $\rho\Omega_s^2$ in Eqs. (12) and (13), where the influence of ρ is of first order and the influence of Ω_s is of second order. Furthermore, $\rho\Omega_s^2 = m_2\omega_2^2/(m_1\omega_1^2) = k_2/k_1$. By analyzing this term along with the results obtained in this section, it is concluded that a softer inner beam in comparison to the outer beam results in a more complex equilibrium state characterized by multistability, while stiffening the inner beam leads to bistability.

Fig. 7 presents an illustrative representation of the four possible stable equilibrium states of the system. As depicted in Figs. 7a and 7b, the stable positions that persists under all stability configurations (SEP_1 and SEP_2) can be observed, while Figs. 7c and 7d show the stable positions that vanish at elevated values of Ω_s (SEP_3 and SEP_4) according to this model.

4. Dynamical analysis

This section presents a comprehensive analysis of the nonlinear dynamics and performance of the proposed harvester. A general overview of its characteristics within the external excitation parameter domain is displayed and comparisons among different configurations of the proposed harvester and the classical bistable are performed.

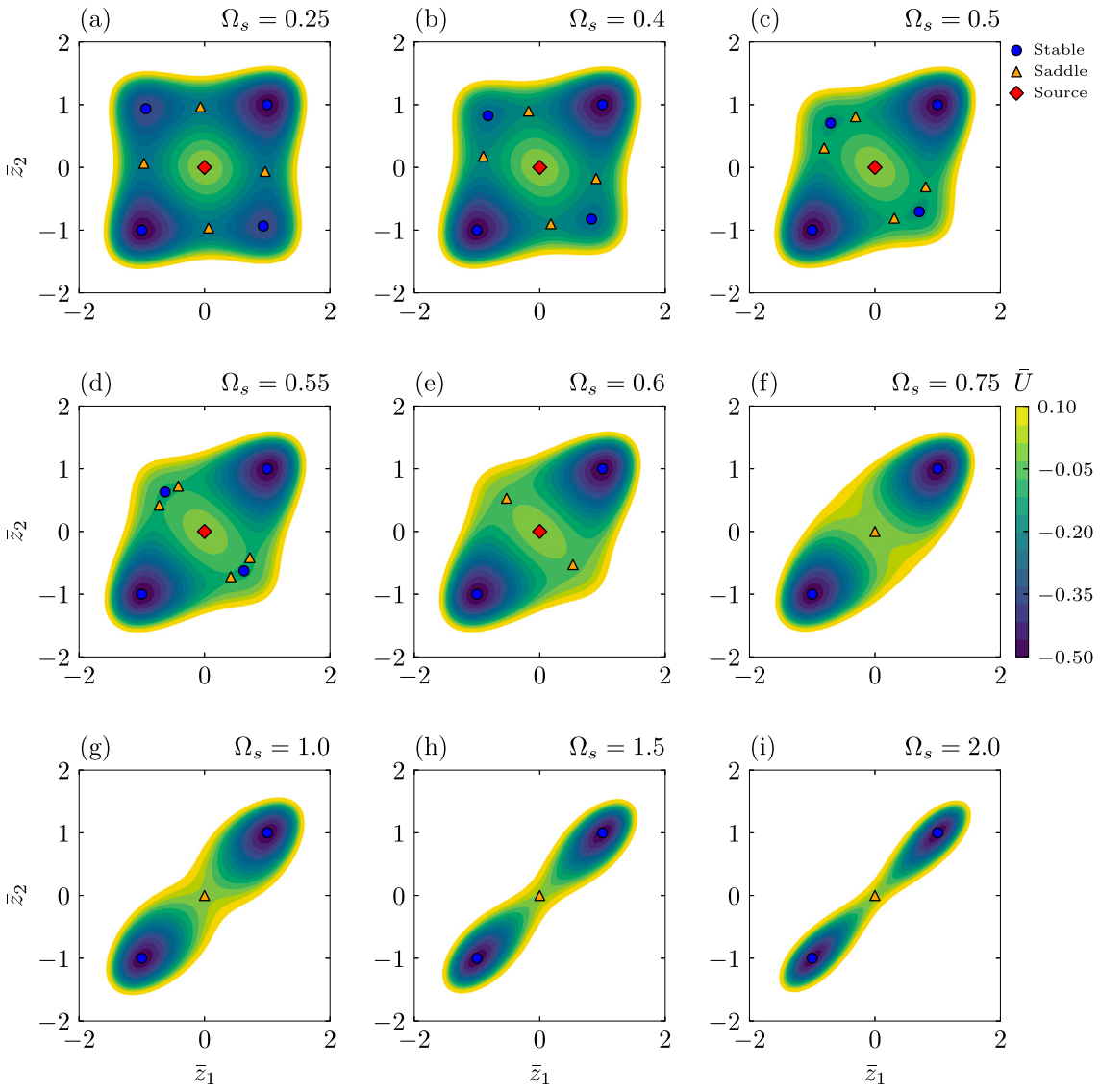

Fig. 3. Equilibrium configurations for a set of Ω_s values, considering a fix mass ratio value of $\rho = 1$. The colorbar indicates the level of potential energy for each combination of system positions $\bar{z}_1$ and $\bar{z}_2$, while blue dots represent stable equilibrium positions, orange triangles represent unstable saddle-type equilibrium positions and red polygons represent unstable source-type equilibrium positions.

4.1. Nonlinear characteristics and performance

The stability analysis shows that stiffening the inner beam with respect to the outer beam completely changes the stability characteristics of the system. By changing either the value of ρ or the value of Ω_s, it tends to converge to the same result at different rates. Therefore, in a dynamical perspective, it is reasonable to vary one parameter keeping the other constant.

A harmonic excitation displacement of the form $\bar{z}_b = \gamma \sin(\Omega\tau)$ is adopted to represent the available ambient mechanical energy, being γ the normalized excitation amplitude, and Ω the normalized excitation frequency. Numerical analyses are carried out by evaluating the influence of the linearized natural frequency ratio parameter, Ω_s, with a constant $\rho = 1$. The other parameters are summarized in Table 1. The analyses are based on three types of diagrams in the $\gamma \times \Omega$ parameter domain: the dynamical responses diagram (DRD) that identifies different kinds of dynamical responses; the Lyapunov exponent diagram (LED) that exhibits the magnitude of the Lyapunov exponents; and the average output power diagram (OPD) that shows the steady state average electrical output power under excitation conditions. The diagrams are built with a grid of 1000 × 1000 sample points, each of which is obtained from a time series integration considering an integration time step $\Delta\tau \propto 2\pi/\Omega$.

The analysis is carried out selecting two specific system configurations based on their stability characteristics: the first configuration features 4 stable equilibrium points, being characterized by $\Omega_s = 0.25$; the second configuration has 2 stable equilibrium points, being represented by $\Omega_s = 1.0$. The initial conditions are $[\bar{z}_1(0), \dot{\bar{z}}_1(0), \bar{z}_2(0), \dot{\bar{z}}_2(0), \bar{v}_1(0), \bar{v}_2(0)] = [1, 0, 1, 0, 0, 0]$, which correspond to SEP_2, a stable position that persists throughout all stability configurations. By means of these diagrams, a comprehensive overview of the system dynamical characteristics and performance at different operational conditions are elucidated.

Different periodicities are classified by colors, considering that T represents the excitation period: dark gray (1T), yellow (2T), green (3T), orange (4T) and purple (5T). Light blue is employed to represent responses with a period equal or greater than 6T, which means multiple periods (MP). Red regions represent chaotic (CH) responses, while dark red regions represent hyperchaotic (HC) responses. These responses can be referred to as dynamical attractors since they represent either stable closed orbits or strange attractors. All classifications are based

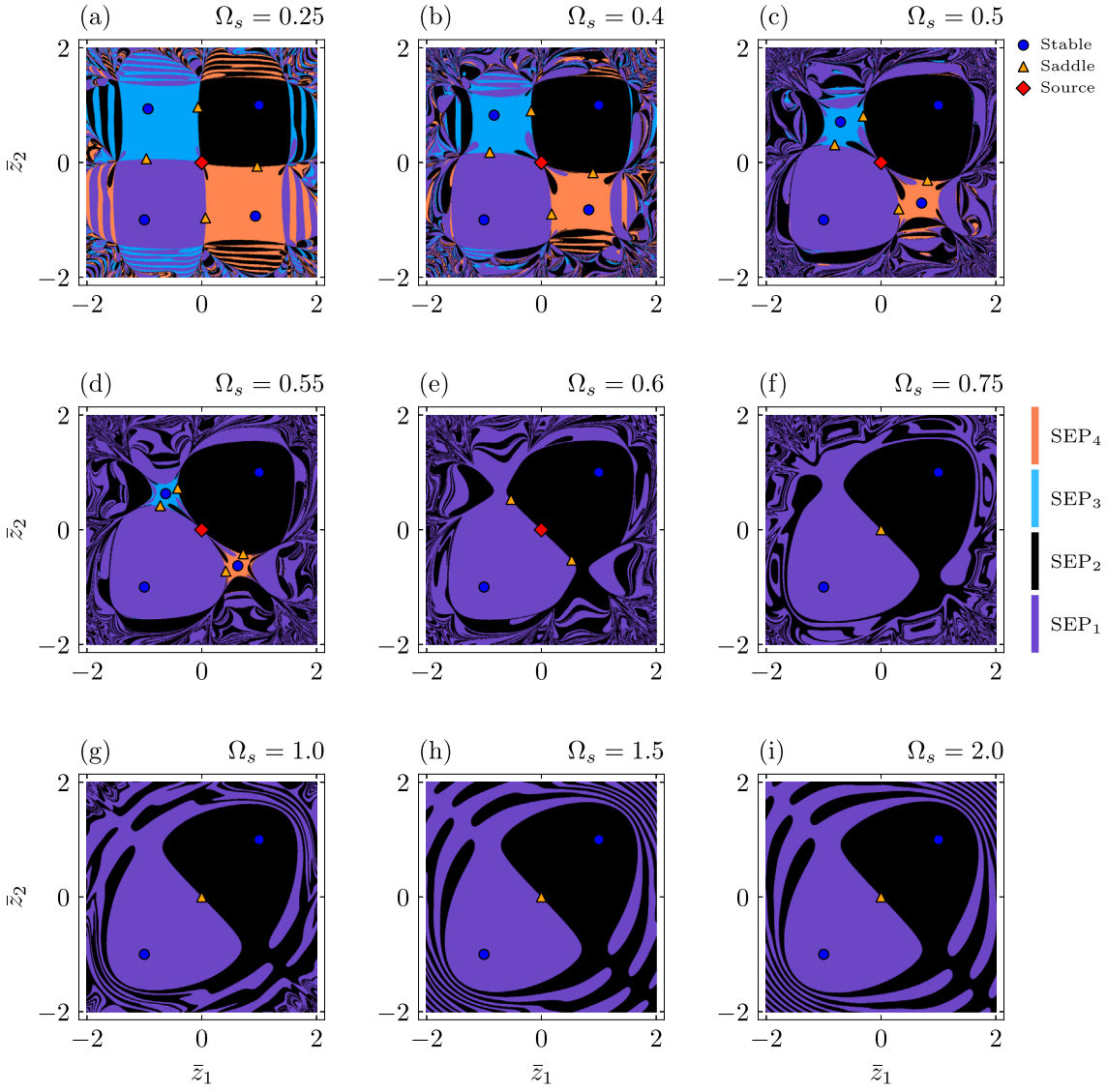

Fig. 4. Basins of attraction for a set of Ω_s values, considering a fix mass ratio value of $\rho = 1$. Colors indicate the stable position the system is attracted to for each combination of initial system positions $\bar{z}_1$ and $\bar{z}_2$, while blue dots represent stable equilibrium positions, orange triangles represent unstable saddle-type equilibrium positions and red polygons represent unstable source-type equilibrium positions. A grid of 2000 × 2000 points was used.

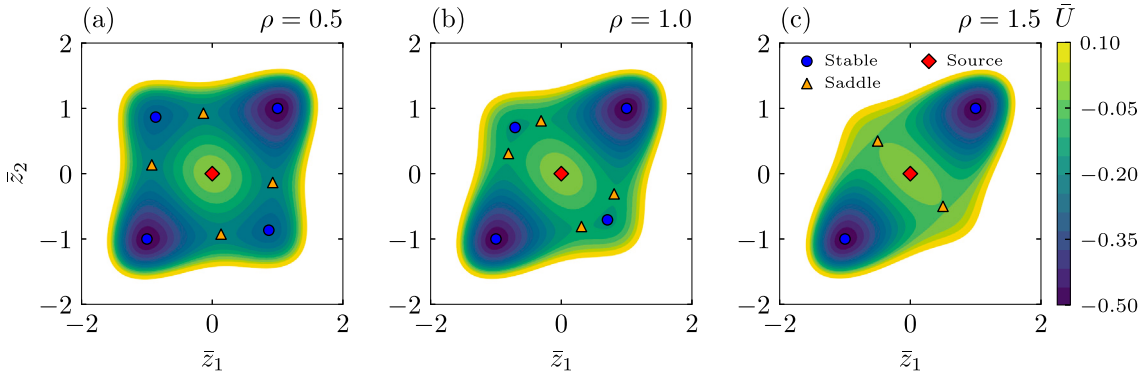

Fig. 5. Equilibrium configurations for a set of ρ values, considering a fix mass ratio value of $\Omega_s = 0.5$. The colorbar indicates the level of potential energy for each combination of system positions $\bar{z}_1$ and $\bar{z}_2$, while blue dots represent stable equilibrium positions, orange triangles represent unstable saddle-type equilibrium positions and red polygons represent unstable source-type equilibrium positions.

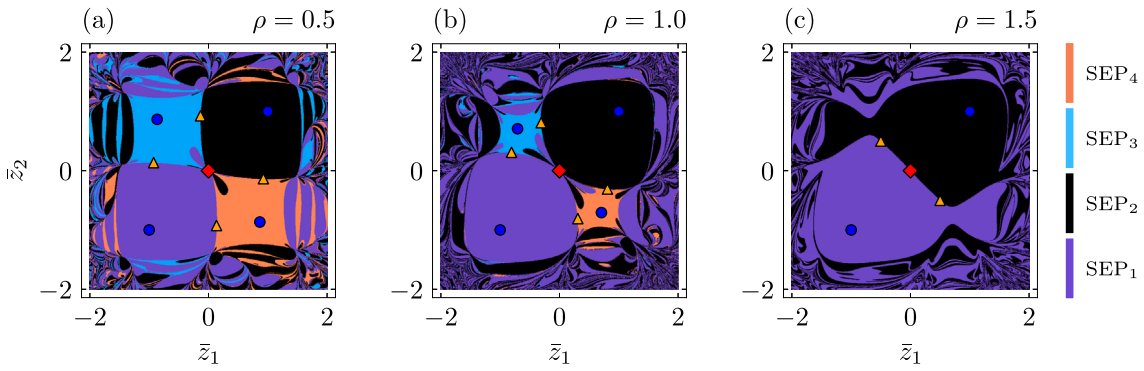

Fig. 6. Basins of attraction for a set of ρ values, considering a fix mass ratio value of $\Omega_s = 0.5$. Colors indicate the stable position the system is attracted to for each combination of initial system positions $\bar{z}_1$ and $\bar{z}_2$, while blue dots represent stable equilibrium positions, orange triangles represent unstable saddle-type equilibrium positions and red polygons represent unstable source-type equilibrium positions. A grid of 2000 × 2000 points was used.

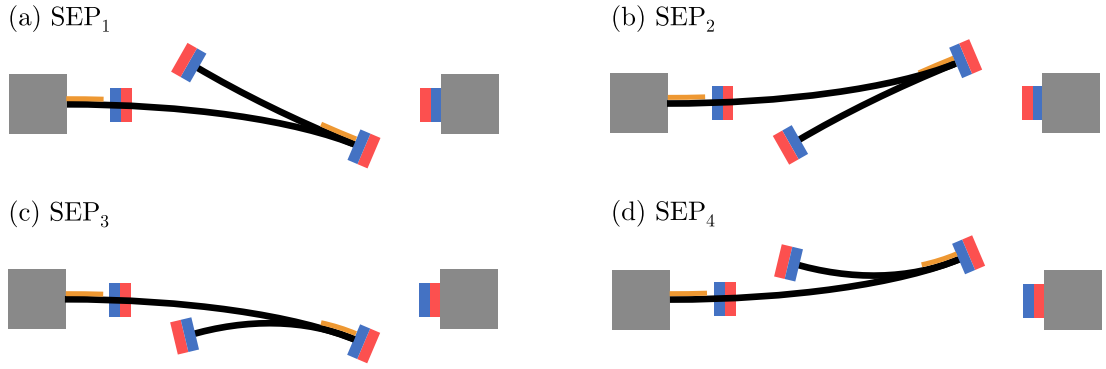

Fig. 7. Representation of the four possible stable equilibrium states of the system: (a) SEP$_1$, (b) SEP$_2$, (c) SEP$_3$ and (d) SEP$_4$.

on the Lyapunov exponents and on the verification of the steady state Poincaré map. By combining these two approaches, the vast majority of dynamical attractors are properly classified, with the outliers being samples that are still converging to a stable orbit at the final time of integration, τ_f.

The Lyapunov exponent, $\lambda_i (i = 1, \ldots, 6)$, spectrum is analyzed employing the method proposed by Wolf et al. [75]. In order to have a proper convergence, 4000 excitation periods (4000T), are imposed at each integration, of wich the last 500 are considered to be the steady state. Additionally, two distinct initial time stages are considered: $\tau_0 = 0$ and $\tau_0 = 0.875\tau_f$ (steady state) to ensure convergence of the Lyapunov exponents on time series samples that exhibit long-term transient chaos orbits. τ_f represents the final time of integration. Concerning Lyapunov exponent colors, rainbow colors represent positive exponents and grayscale colors represent negative exponents.

Figs. 8–10 depict examples of DRDs and LEDs for the two treated configurations. Examples of the dynamical attractor for each configuration are depicted in Figs. 8 and 9, just below the corresponding DRDs. The chosen examples are identified by white circles with numbered labels within the DRDs. These labels represent the three phase subspaces ($\bar{z}_1 \times \bar{z}_2$, $\bar{z}_1 \times \dot{\bar{z}}_1$ and $\bar{z}_2 \times \dot{\bar{z}}_2$) of the system's steady state response, which are plotted, labeled, and color-coded according to the attractor designation in the DRDs. The Poincaré maps are depicted as dots in each phase subspace and the equilibrium positions discussed in Section 3 are useful for spatial references in the $\bar{z}_1 \times \bar{z}_2$ phase subspaces.

For the case of $\Omega_s = 0.25$, the orbits with periods of 2T, 3T and 4T are observed to be trapped around SEP$_2$, indicating that the system lacks sufficient energy to overcome the local potential energy minima (potential energy well). In contrast, the remaining examples display orbits with high amplitude displacements. The orbits with periods of 1T and 5T are characterized by synchronized or nearly synchronized behavior, where $\bar{z}_1$ and $\bar{z}_2$ show a coordinated motion, causing the system to oscillate around only three equilibrium positions. Conversely, the orbits characterized by multiple periods (MP), chaos (CH) and hyperchaos (HC) exhibit desynchronized or complex behavior, leading the system to visit all possible equilibrium points.

The case with $\Omega_s = 1.0$ reveals that the example orbits with periods of 1T and 5T are trapped around stable equilibrium positions, with the 5T orbit being confined around SEP$_2$, and the 1T orbit being confined around SEP$_1$. In general (for any case of Ω_s), this suggests that the system dynamics may start at one stable equilibrium position (SEP$_2$) and end up being trapped around another (SEP$_1$) due to transient motion. The remaining periodic example orbits show high amplitude displacements and visit all the equilibrium positions, leading to synchronized or nearly synchronized behavior as depicted in the phase subspaces $\bar{z}_1 \times \dot{\bar{z}}_1$ and $\bar{z}_2 \times \dot{\bar{z}}_2$ of each example. The chaotic (CH) and hyperchaotic (HC) examples, similar to previous cases, also show high amplitude displacements and exhibit desynchronized or complex behavior. Therefore, an effort was made to select orbits that differed from those chosen in the previous case, highlighting that these classified dynamical attractors merely indicate the periodicity of motion, and not necessarily the amplitude of motion or complex behaviors as synchronization.

Finally, it is also important to note that the distinction between chaotic and hyperchaotic attractors is based on the number of instability directions. Chaotic attractors are represented by a single positive Lyapunov exponent ($\lambda_1 > 0$) with the remaining being negative, whereas hyperchaotic attractors have at least two positive exponents ($\lambda_1 > 0$ and $\lambda_2 > 0$). This can be observed in the Lyapunov Exponent Diagrams (LEDs) presented in Fig. 10.

Energy harvesting performance is now in focus. Fig. 11 presents the average output power diagrams (OPDs) for the two configurations of $\Omega_s = 0.25$ and $\Omega_s = 1.0$. The OPDs are divided into six subfigures, with Figs. 11a and 11b showing the contribution of the first

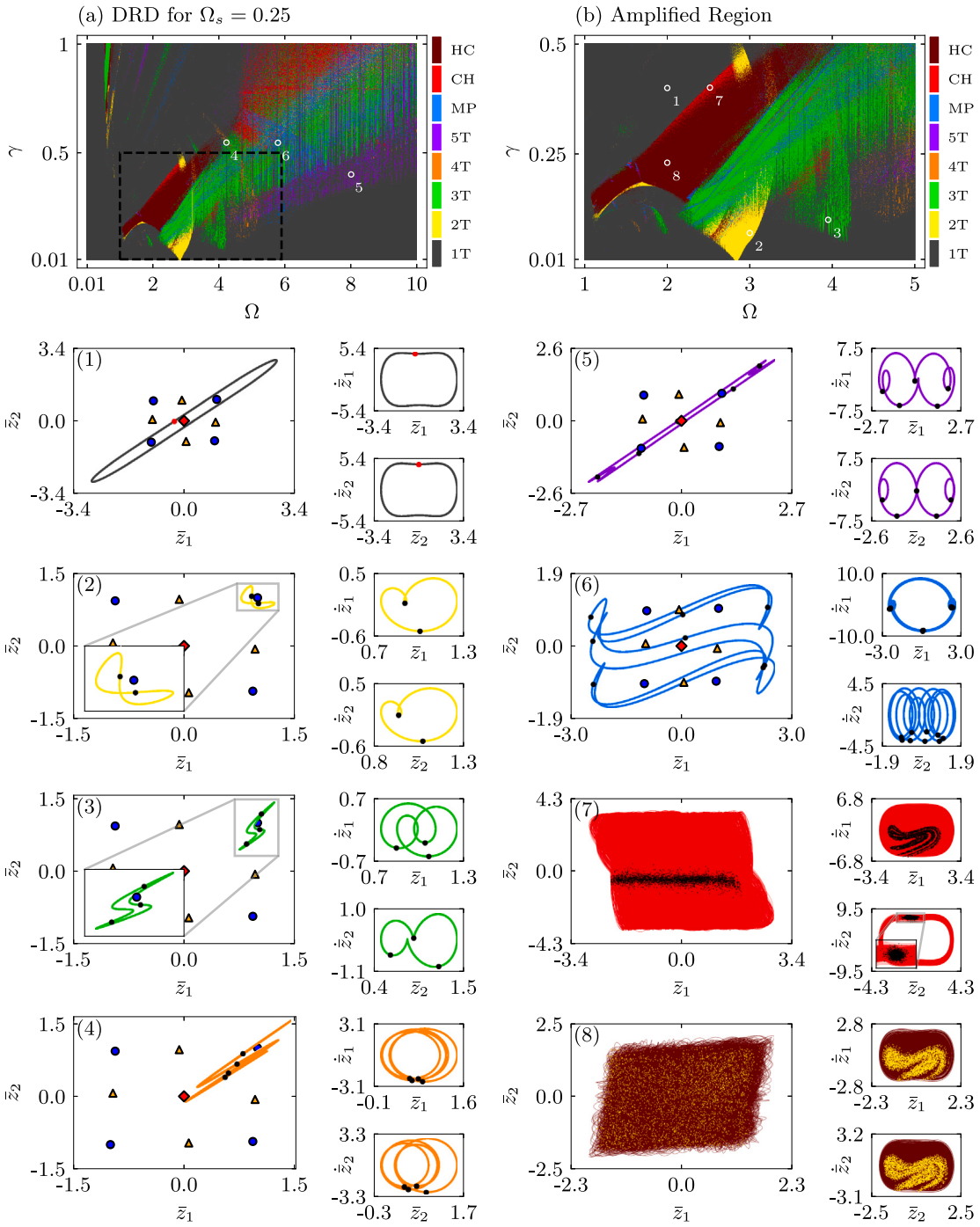

Fig. 8. (a) Dynamical Response Diagrams (DRD) for a configuration with 4 stable and 5 unstable equilibrium points ($\Omega_s = 0.25$). (b) Amplified region delimited by the black dashed square in (a). Each color represent a dynamical attractor as described in text. White circles followed by numbers in (a) and (b) represent examples of the attractors contained in the DRD. Three phase subspaces of the system's steady state response ($\bar{z}_1 \times \bar{z}_2$, $\bar{z}_1 \times \dot{\bar{z}}_1$ and $\bar{z}_2 \times \dot{\bar{z}}_2$) are plotted, colored and numbered according to the respective attractor marked in the DRDs. Poincaré maps are also plotted in each subspace by red dots for 1T attractor, by yellow dots for the HC attractor, and by black dots for 2T, 3T, 4T, 5T, MP and CH attractors. Equilibrium points are inserted as spatial reference in the $\bar{z}_1 \times \bar{z}_2$ phase subspaces. A grid of 1000 × 1000 points was used in each DRD.

degree of freedom to the performance, Figs. 11c and 11d displaying the contribution of the second degree of freedom, and Figs. 11e and 11f showing the overall average output power converted by the harvester. The accompanying colorbars illustrate the quality of performance, with blue to red hues indicating good performance and purple hues indicating poor performance, as defined by the colormap. To facilitate interpretation, the range of each colorbar is restricted to a specific limit value. The uppermost value on the peak of the top colorbar arrow represents the maximum average output power attained by the harvester.

For the case of $\Omega_s = 0.25$, the first degree of freedom exerts greater influence in a large region in the parameter domain, and the second displays a considerable contribution in higher frequencies. The region B, delimited by the white dashed polygon, shows a scenario where the second degree of freedom presents high performance, while the first degree of freedom shows less performance, which illustrates a circumstance of transmissibility of energy within the system. In contrast, both

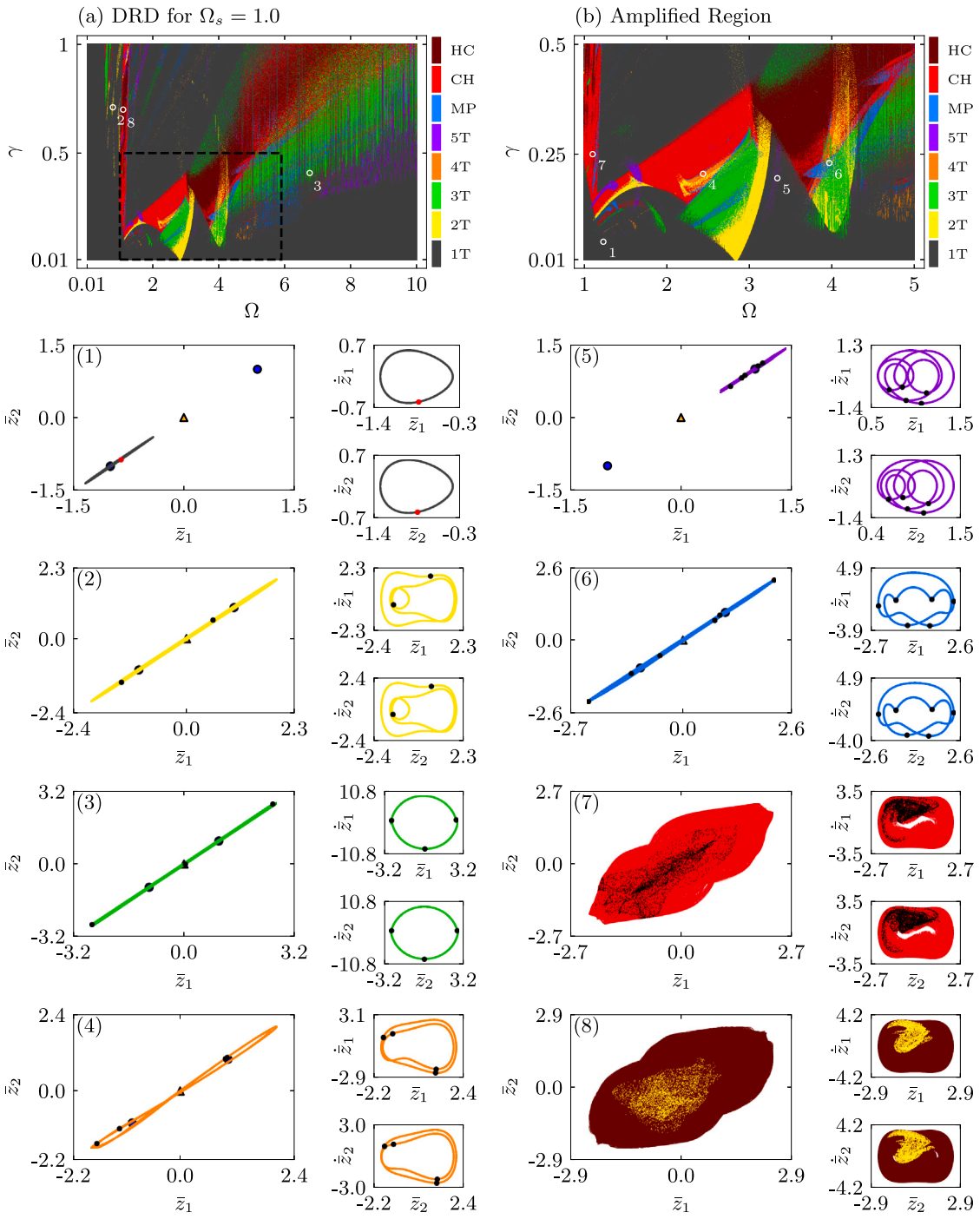

Fig. 9. (a) Dynamical Response Diagrams (DRD) for a configuration with 2 stable and 1 unstable equilibrium points ($\Omega_s = 1.0$). (b) Amplified region delimited by the black dashed square in (a). Each color represent a dynamical attractor as described in text. White circles followed by numbers in (a) and (b) represent examples of the attractors contained in the DRD. Three phase subspaces of the system's steady state response ($\bar{z}_1 \times \bar{z}_2$, $\bar{z}_1 \times \dot{\bar{z}}_1$ and $\bar{z}_2 \times \dot{\bar{z}}_2$) are plotted, colored and numbered according to the respective attractor marked in the DRDs. Poincaré maps are also plotted in each subspace by red dots for 1T attractor, by yellow dots for the HC attractor, and by black dots for 2T, 3T, 4T, 5T, MP and CH attractors. Equilibrium points are inserted as spatial reference in the $\bar{z}_1 \times \bar{z}_2$ phase subspaces. A grid of 1000 × 1000 points was used in each DRD.

degrees-of-freedom contribute effectively in the region A, delimited by the black dashed rectangle. This result can be seen in the overall OPD in Fig. 11e. In this region, hyperchaotic and periodic 3T attractors are predominant according to Fig. 8.

In the second case of $\Omega_s = 1.0$, a similar scenario can be observed where the first degree of freedom exerts greater influence in the performance and the second displays a good contribution in higher frequencies and in a small frequency band in low frequencies. Similarly to the previous case, the region D, delimited by a black dashed rectangle, is characterized by the effective contribution of both degrees-of-freedom to the performance, while the white dashed region, E, demonstrates a scenario in which only the first degree of freedom contributes effectively to the power conversion. The predominant attractors of these regions are 1T and chaotic according to Fig. 9.

In terms of maximum output power, the case which $\Omega_s = 1.0$ performs better, although the points of very high performance (near $\bar{P}_{\text{avg}}^{(\max)}$) for the second DoF are scarce. In contrast, the areas with high performance of the second DoF in the case of $\Omega_s = 0.25$ are

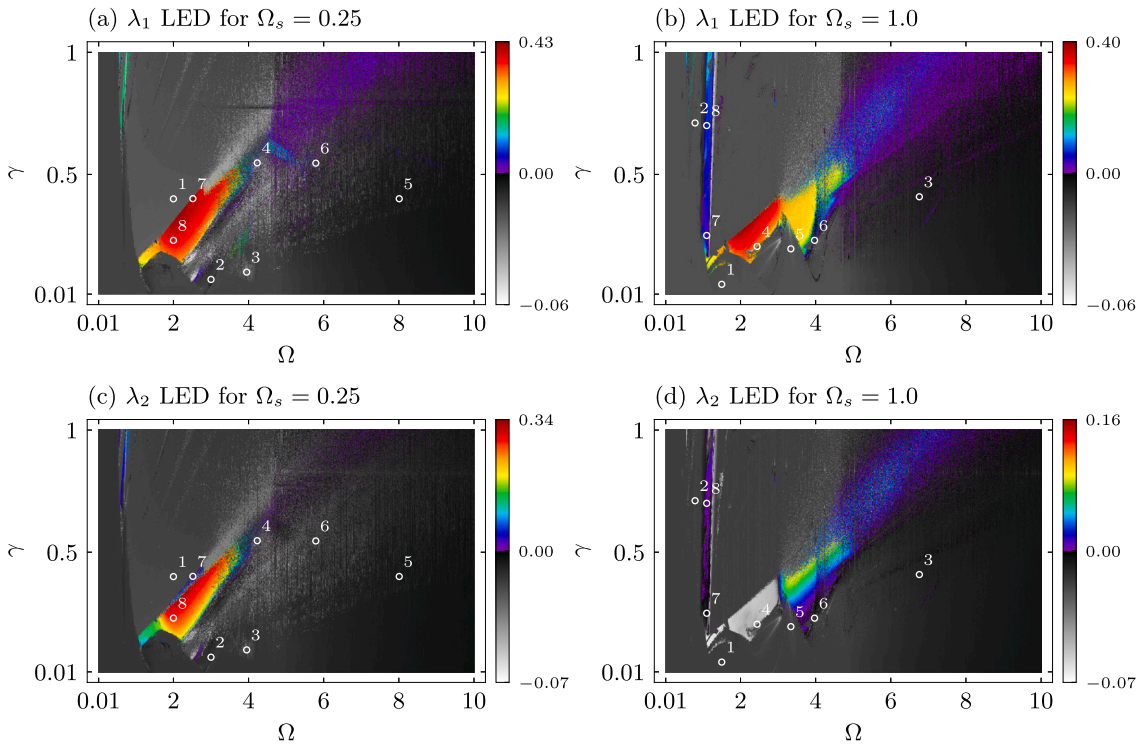

Fig. 10. Lyapunov Exponent Diagrams (LEDs) for the two largest exponents (λ_1 and λ_2) for each case of Ω_s: (a) λ_1 for $\Omega_s = 0.25$, (b) λ_1 for $\Omega_s = 1.0$, (c) λ_2 for $\Omega_s = 0.25$, and (d) λ_2 for $\Omega_s = 1.0$. Rainbow colors represent positive exponents, while grayscale colors represent negative exponents. White circles followed by numbers represent the attractors exemplified in Figs. 8 and 9. A grid of 1000 × 1000 points was used in each LED.

more consistent. In general, the best overall power output regions of the two cases are similar. The yellow dashed areas labeled as C and F, respectively for each case, are characterized by a portion of intermittent irregular sparse points of high and low performance. This is a characteristic of nonlinear systems that exhibit multiple solutions based on its initial conditions. This complexity is further illustrated by the DRDs in Figs. 8 and 9, displaying a high probability of two or more attractors arising in these areas, instead of a concise area of a single dynamical attractor. In these areas, the knowledge of the probability of a dynamical attractor to arise in each point of the diagram combined with a suitable smart control system need to be incorporated into the system to ensure dynamical stability in these high performance attractors at operation conditions.

Points were marked in Fig. 11 for each white and black dashed areas to exemplify the dynamics of interest of each region. Fig. 12 displays the steady state time series for the positions $\bar{z}_1$ and $\bar{z}_2$, the relative position $\bar{z}_2 - \bar{z}_1$, and the output voltages $\bar{v}_1$ and $\bar{v}_2$ for each of these points. Plots (1) and (3) illustrate the behavior in which both degrees of freedom contribute effectively for the power conversion (black dashed regions A and D, respectively), while plots (2) and (4) exemplify the behavior in which only one degree of freedom contribute effectively for the power conversion (white dashed regions B and E, respectively). In general, these examples indicate that the energy conversion is proportional to the displacements: the output voltage $\bar{v}_1$ is proportional to the displacement of the first DoF $\bar{z}_1$, while the output voltage $\bar{v}_2$ is proportional to the relative position, $\bar{z}_{\text{rel}} = \bar{z}_2 - \bar{z}_1$. This is expected as it is tangible to imagine that the resulting strain in the piezoelectric element of the second DoF depends on the relative position between DoFs, suggesting that in-phase synchronization between DoFs, that is, when the outer beam is moving upwards and the outer beam is moving downwards, makes only one DoF contribute effectively in the power conversion, while desynchronized, out-of-phase and anti-phase synchronized behavior makes the two DoFs contribute effectively in the power conversion. The way the system behaves in these cases are closely related to the linear modes of vibration of the structure, which are exemplified in Fig. 13.

To further investigate the regions with high performance, the maximum power output, $\bar{P}_{\text{avg}}^{(\max)}$, for each value of excitation amplitude, γ, is marked as colorful points in the OPDs as shown in Figs. 14a and 14b for the cases of $\Omega_s = 0.25$ and $\Omega_s = 1.0$, respectively. Grayscale colors represent the OPD for reference. The colorbar next to the OPDs represent the value of the average output power of each point of maximum. For $\Omega_s = 0.25$, it is observed that $\bar{P}_{\text{avg}}^{(\max)}$ steadily grows as γ increases, with a larger occupation of the diagram. In addition, the region between $\Omega \approx 4 \rightarrow 7$ exhibits the maximum values of output power. In contrast, for $\Omega = 1.0$, the values of $\bar{P}_{\text{avg}}^{(\max)}$ are concentrated in the $\Omega \approx 1 \rightarrow 7$ interval of excitation frequency, with the maximum values occurring in a similar range of frequencies as the previous case.

Constant values of γ are selected in each diagram, labeled as G ($\gamma \approx 0.2$), H ($\gamma \approx 0.6$) and I ($\gamma \approx 0.9$) for the $\Omega_s = 0.25$ case, and J ($\gamma \approx 0.1$), K ($\gamma \approx 0.3$) and L ($\gamma \approx 0.5$) for the $\Omega_s = 1.0$ case. They are displayed in Figs. 14c and 14d, showing similar bandwidths of operation. Three points of maximum output power for each case are marked with red circles and labeled with a number of 1 to 3. The three phase subspaces ($\bar{z}_1 \times \bar{z}_2$, $\bar{z}_1 \times \dot{\bar{z}}_1$ and $\bar{z}_2 \times \dot{\bar{z}}_2$) and their respective Poincaré maps are displayed below each case, labeled according to their respective point of maximum. The colors of the phase subspaces correspond to the dynamical attractors classified in Figs. 8 and 9 and the respective equilibrium points of each case are included as a spatial reference in the $\bar{z}_1 \times \bar{z}_2$ phase subspaces. These results show that the regions of high performance are characterized by a high amplitude displacement of each degree of freedom of the proposed harvester that courses around or through all equilibrium positions. However, point 1, which exhibits the $\bar{P}_{\text{avg}}^{(\max)}$ orbits for $\gamma \approx 0.1$, shows an exception to this statement, where the system does not have enough input energy to overcome the system potential barriers, being trapped around the stable equilibrium position. This represents a worst-case scenario for this

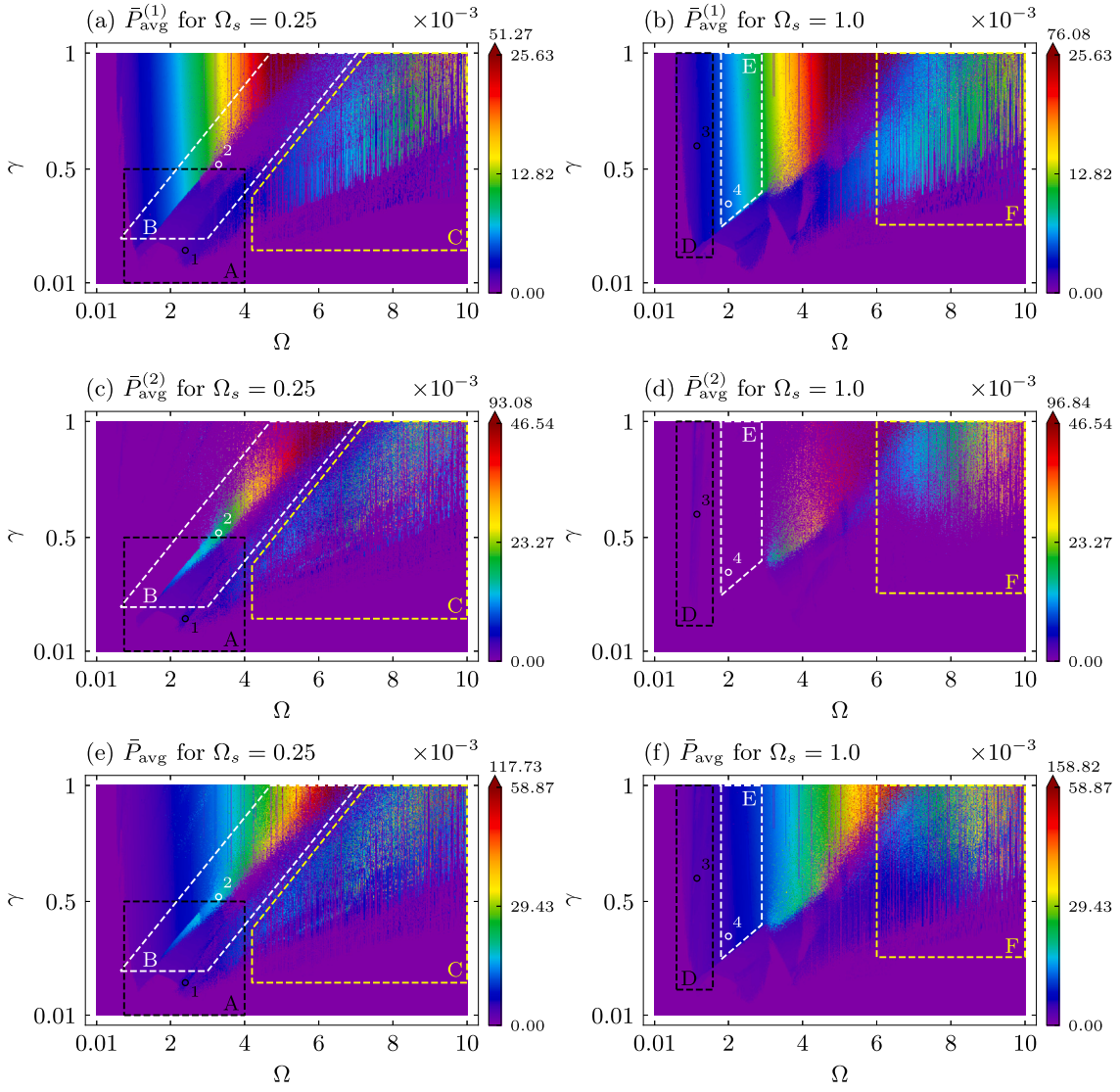

Fig. 11. Average Output Power Diagrams (OPDs) for two different parameters: $\Omega_s = 0.25$ (first column) and $\Omega = 1.0$ (second column). The first row displays the contribution of the first degree of freedom to the average output power, while the second row shows the contribution of the second degree of freedom. The third row displays the overall average output power of the harvester for each value of Ω_s. The areas defined by dashed polygons and numbered circles are discussed in the text.

type of harvester, presenting low power output, and is a characteristic present in several classical multistable harvesters in the literature.

In order to comprehensively characterize the high-performance dynamics of the harvester, the analysis presented in Figs. 14 are extended to encompass a broader range of values for the parameter Ω_s. For each value of Ω_s, the points of maximum average output power as a function of γ are selected, and for each one of these points, the corresponding dynamical attractor is carefully accounted. Results of this investigation are summarized in Fig. 15, which provides a comprehensive overview of the occurrence of each dynamical attractor in points of maximum performance. It is observed that for cases where the harvester exhibits 9 equilibrium positions ($\Omega_s < 0.75$), maximum performance characteristics are associated with 3T attractors, followed by 1T attractors. While 2T and 5T, as well as high periodic (MP) and aperiodic (CH and HC) attractors, also occur, they are not predominant. In contrast, for systems with 3 equilibrium states ($\Omega_s \geq 0.75$), the predominance of 3T attractor decreases, while the occurrence of MP, CH and HC attractors increases. Notably, 2T, 4T and 5T attractors almost never appear in any of the cases studied.

4.2. Performance comparisons

In this section, comparisons between the performances of two harvesters are presented. The comparisons are based on the percentage difference, denoted as $\Delta\bar{P}_{\text{avg}}(\%)$, between the average output power of each harvester ($\bar{P}^{(\text{M2DoFH})}_{\text{avg}}$ and $\bar{P}^{(\text{CBH})}_{\text{avg}}$), where M2DoFH refer to the proposed multistable harvester in this work and CBH is the classical bistable harvester. Eq. (17) is used to calculate the percentage difference, which allows a classification based on three sets:

- $\Delta\bar{P}_{\text{avg}}(\%) > 0$: M2DoFH shows better performance;
- $\Delta\bar{P}_{\text{avg}}(\%) = 0$: M2DoFH and CBH shows the same performance;
- $\Delta\bar{P}_{\text{avg}}(\%) < 0$: CBH shows better performance.

$$\Delta\bar{P}_{\text{avg}}(\%) = \frac{\bar{P}^{(\text{M2DoFH})}_{\text{avg}} - \bar{P}^{(\text{CBH})}_{\text{avg}}}{\bar{P}^{(\text{CBH})}_{\text{avg}}} \times 100. \tag{17}$$

On this basis, this estimation is applied to each point of the 1000×1000 OPD grid of each harvester, resulting in a performance comparison diagram (PCD).

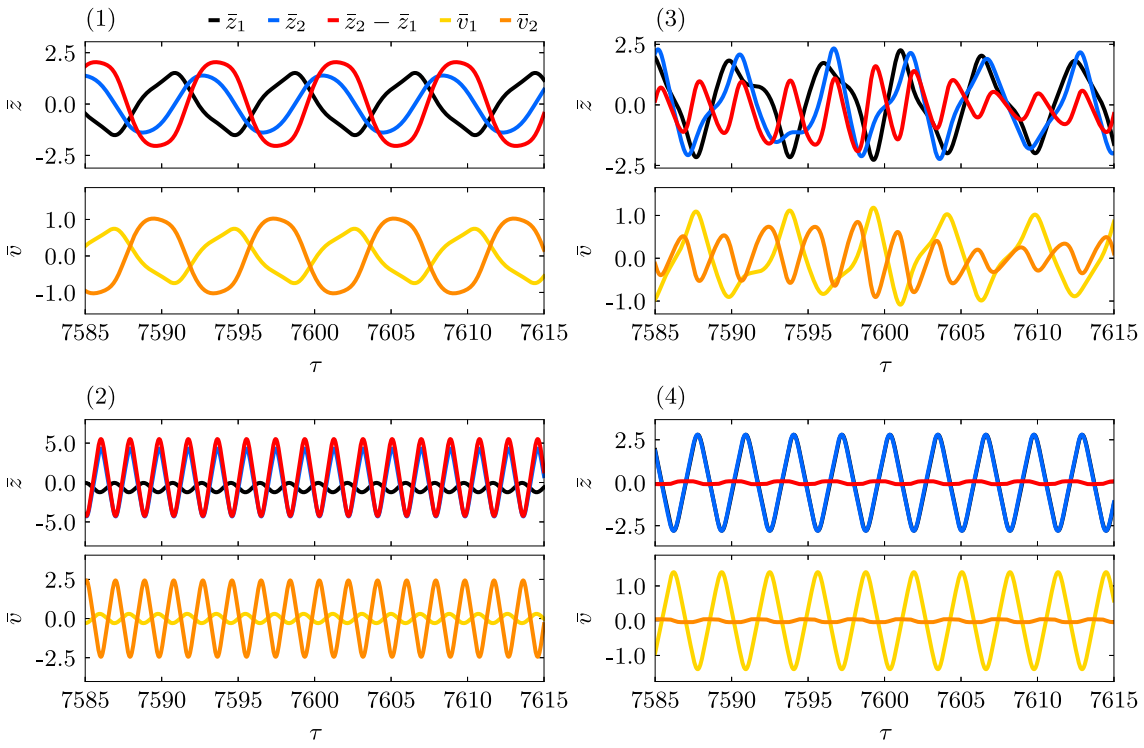

Fig. 12. Steady state timeseries of each numbered point marked in Fig. 11. The positions $\bar{z}_1$ and $\bar{z}_2$, the relative position $\bar{z}_2 - \bar{z}_1$, and the output voltages $\bar{v}_1$ and $\bar{v}_1$ and $\bar{v}_2$ are plotted and colored according to legend. Each one of the four groups of plots are numbered according to the respective point marked in the OPDs.

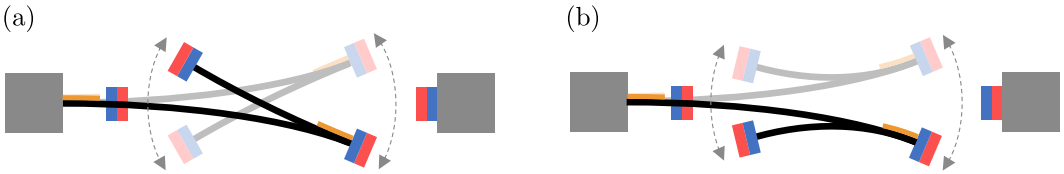

Fig. 13. Representation of the possible linear vibration modes of the system.

4.2.1. *Multistable 2-DoF vs classical bistable*

The overall characteristics of the classical bistable energy harvester is analyzed by considering the same approach employed for the 2-DoF system, building DRD and OPD by setting the parameters of the second degree of freedom to zero ($\alpha_2 = \beta 2 = \zeta_2 = \rho = \Omega_s = \chi_2 = \varphi_2 = \kappa_2 = 0$). Results observed in Fig. 16 show consistent regions of dynamical attractors at lower excitation frequencies and sparser regions at higher frequencies, with the 1T, 3T, and CH being the predominant dynamical attractors in the DRD. Qualitatively, the OPD in Fig. 16b displays a similar structure compared to the multistable 2-DoF harvester, showing however, lower maximum average output power: while the classical bistable harvester displays a maximum $\bar{P}_{\text{avg}} = 65.92$, the multistable harvester converts up to $\bar{P}_{\text{avg}} = 117.73$ with $\Omega_s = 0.25$, and $\bar{P}_{\text{avg}} = 158.82$ with $\Omega_s = 1.0$, an performance enhancement of 78.6% and 140.92%, respectively.

An overall comparison of the performance of the classical bistable energy harvester with the multistable 2-DoF energy harvester is established considering eight configurations related to the value of Ω_s: 0.25, 0.5, 0.75, 1.0, 1.25, 1.5, 1.75, 2.0. The performance comparison diagrams (PCD) in Fig. 17 illustrate the analysis, where red colors indicate regions in which the multistable 2-DoF energy harvester outperforms the classical bistable energy harvester, and black colors indicate regions where the classical bistable energy harvester performs better. To better illustrate the difference between the two harvesters, the colorbar limits are truncated by 50%. In other words, the darker colors in each red or black colormap represent scenarios in which one harvester outperforms the other by a factor of 50% or more. Theoretically, the limit of the red % is ∞, while the limit of the black values is -100%, as the comparison is done utilizing the classical bistable energy harvester (CBH) as reference, as determined in Eq. (17). Besides, the red areas of the diagram are accounted, represented by A_{red}.

By increasing the value of Ω_s causes the regions where the multistable 2-DoF energy harvester most outperforms the bistable harvester to shift towards higher frequencies, as expected given $\Omega_s = \omega_2/\omega_1$. Moreover, as Ω_s increases, the darker regions representing the narrow frequency ranges where the bistable harvester most outperforms the multistable also become more prominent in higher frequency ranges, augmenting the range of frequencies where the classical bistable harvester outperforms the multistable one in key regions of interest. This can be observed by examining the structures enclosed within the white dashed rectangles showed in the PCDs, which progressively shift towards higher frequencies with increasing Ω_s. Additionally, by increasing Ω_s, it is observed an increase in the area, A_{red}, that represent the better performance of the 2 DoF multistable energy harvester.

Having identified the regions in the excitation parameter domain where the proposed harvester outperforms the classical bistable harvester, it is crucial to evaluate the quality of these regions. To this end, consider the introduction of a normalization of the output power for each output power diagram (OPD) analyzed with different values of $\Omega_s = (0.25, 0.5, 0.75, 1.0, 1.25, 1.5, 1.75, 2.0)$. Specifically, the normalized power, $\bar{P}_{\text{norm}}$, is defined as the ratio of the average output power at each point in the OPD, denoted by $\bar{P}_{\text{avg}}$, to the maximum average output

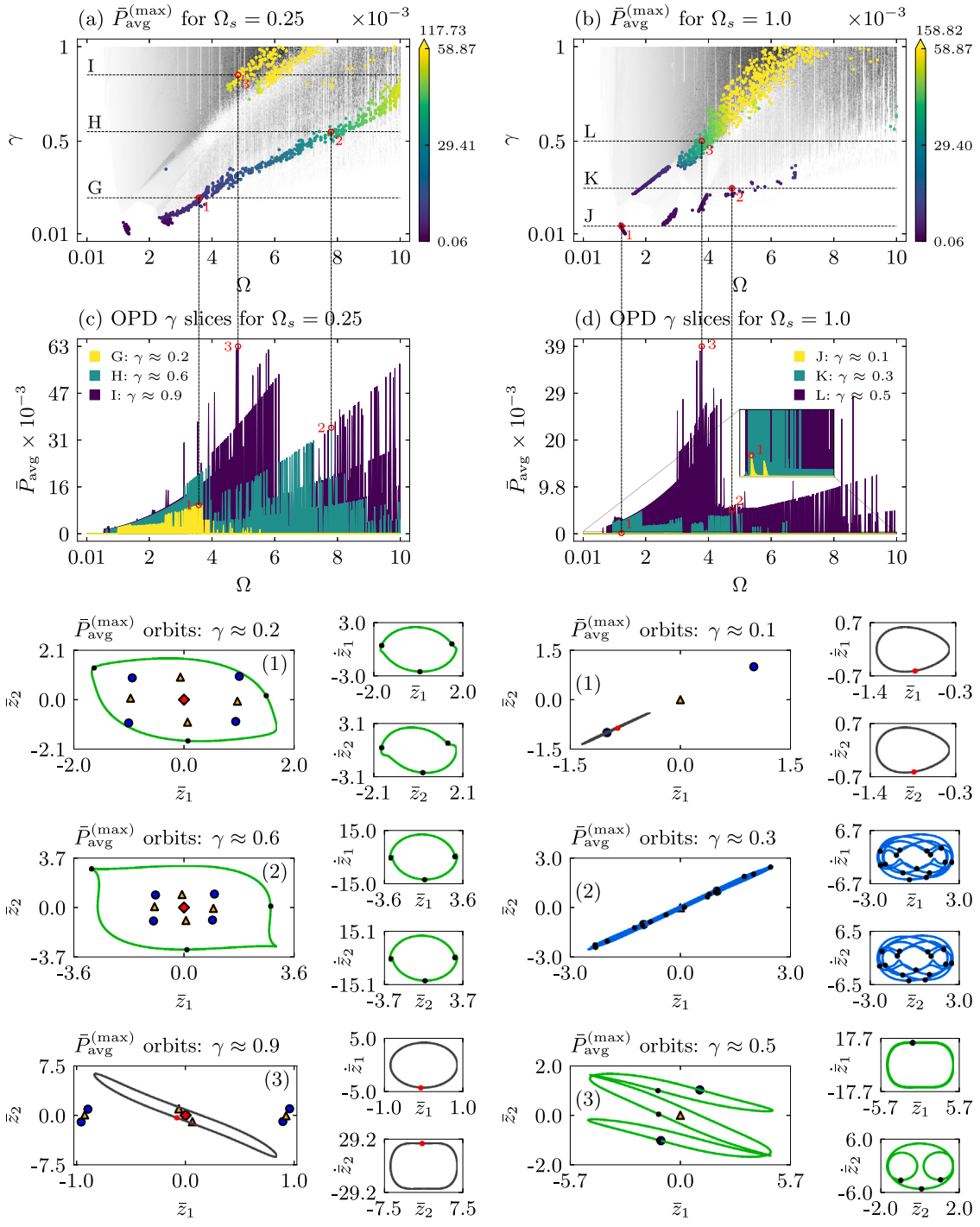

Fig. 14. Maximum average output power as a function of γ for two cases of Ω_s: (a) $\Omega_s = 0.25$ and (b) $\Omega_s = 1.0$. Panels (c) and (d) display the slices G, H, I and J, K, L, respectively, of the output power diagrams (OPDs) for three values of γ in each case, with red circles denoting the maximum power achieved for each slice. Three phase subspaces ($\bar{z}_1 \times \bar{z}_2$, $\bar{z}_1 \times \dot{\bar{z}}_1$ and $\bar{z}_2 \times \dot{\bar{z}}_2$) and Poincaré maps for each case are generated and labeled according to their respective points in the OPDs and provide further insight into the steady state response of the system in high performance conditions. The colors of the phase subspaces correspond to the attractors presented in Figs. 8 and 9, and equilibrium points are included as a reference in the $\bar{z}_1 \times \bar{z}_2$ phase subspaces. To facilitate the visualization, the non-maximum values of the OPD are plotted in grayscale in (a) and (b).

power across all points in that same OPD, denoted by $\bar{P}_{avg}^{(max)}$:

$$\bar{P}_{norm} = \frac{\bar{P}_{avg}}{\bar{P}_{avg}^{(max)}}. \tag{18}$$

This normalization procedure results in all OPDs being scaled to the range $[0, 1]$, providing a qualitative measure of performance for each value of Ω_s. Subsequently, the occurrence of $\bar{P}_{norm} \geq 0.01$ for each case is analyzed, which indicates the instances where the normalized output power is at least 1% of the output power range, while excluding very low power values. The outcome of the analysis is summarized in Fig. 18a, where the occurrence diagram is presented. By analyzing this diagram, four areas of interest can be delimited, as showed in Fig. 18b. The green area denoted by the letter A can be classified as the region with the best performance, exhibiting a high occurrence of good performance. In contrast, the yellow region labeled as B represents the region with many fluctuations due to the presence of intermittent

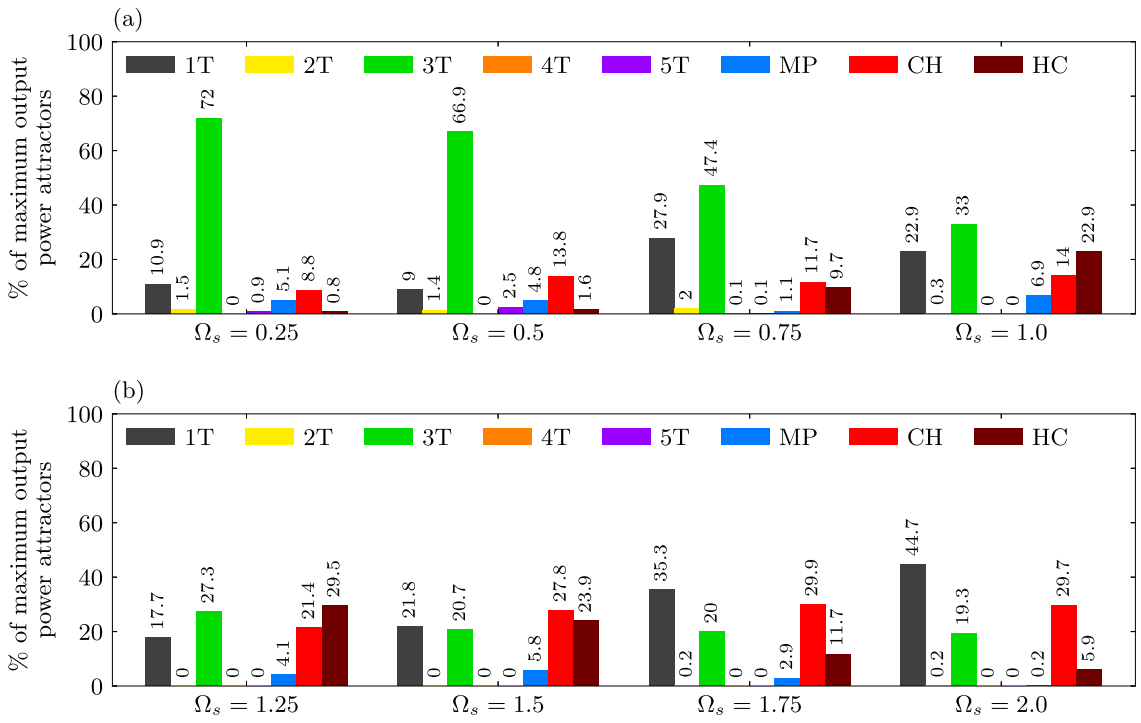

Fig. 15. Characterization of the high-performance dynamics of the harvester: Percentage of occurrence of attractors of the points of maximum average output power as a function of γ for (a) $\Omega_s = \{0.25, 0.5, 0.75, 1.0\}$ and (b) $\Omega_s = \{1.25, 1.5, 1.75, 2.0\}$.

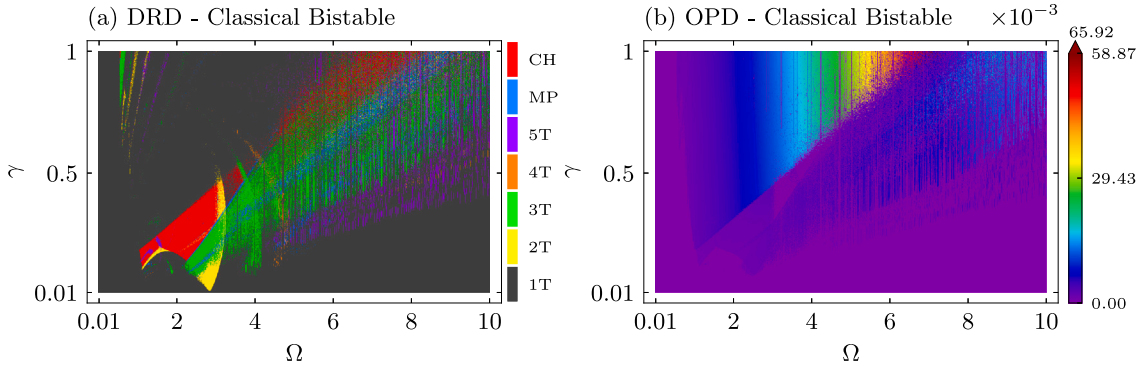

Fig. 16. (a) DRD and (b) OPD for the classical bistable energy harvester. Colors in (a) represent dynamical attractors while colors in (b) represent the average output power of the harvester ($\bar{P}_{\text{avg}}$).

irregular sparse points of high and low performance, caused by the numerous attractors in its basin of attraction. Although region B can present high performance at higher frequencies of operation, it should be classified as a region of moderate performance as it need to be associated with a control scheme to stabilize in a suitable attractor. Region C, represented in orange, is qualitatively similar to region B, but shows lower occurrence in the diagram of Fig. 18a. Lastly, the red region labeled as D is characterized by poor harvester performance and should be avoided in applications of this type of harvester. Therefore regions A, B and C can be classified as regions of interest.

By comparing Figs. 17 and 18, it is clear that, in terms of overall average output power, the multistable 2-DoF energy harvester outperforms the bistable harvester in almost every region of interest. This improved performance can be attributed space-efficient design of the proposed multistable harvester, which is achieved by the incorporation of an inner beam with a second piezoelectric patch.

In contrast, in terms of power density, $\bar{P}^{\text{den}}_{\text{avg}}$, as defined by Eq. (15), the proposed system outperforms the classical bistable energy harvester only in specific zones of the diagram, as depicted in Fig. 19. This is further explicit by the measure of the area in red, A_{red}. These zones are mainly associated with the regions B and C of moderate performance, as classified in Fig. 18b, suggesting that these zones are associated with the high performance of both degrees-of-freedom. This indicates that the transmission of energy from the external source to the structure, and from the structure to the piezoelectric elements is done more efficiently in these regions. In the black zones, the superior performance of the classical bistable harvester can be attributed to the insertion of an additional source of damping by introducing the second degree-of-freedom. In these regions, the extra degree-of-freedom acts as an energy sink that does not transmit the energy efficiently to the transducer element.

4.2.2. *Different 2-DoF multistable configurations*

This subsection establishes a comparison between two different configurations within the group of cases analyzed in this work ($\Omega_s = \{0.25, 0.5, 0.75, 1.0, 1.25, 1.5, 1.75, 2.0\}$). Eq. (17) is used, but instead of comparing with the CBH, now the comparison is done regarding the device with $\Omega_s = 0.25$. Fig. 20 presents a comparison between the

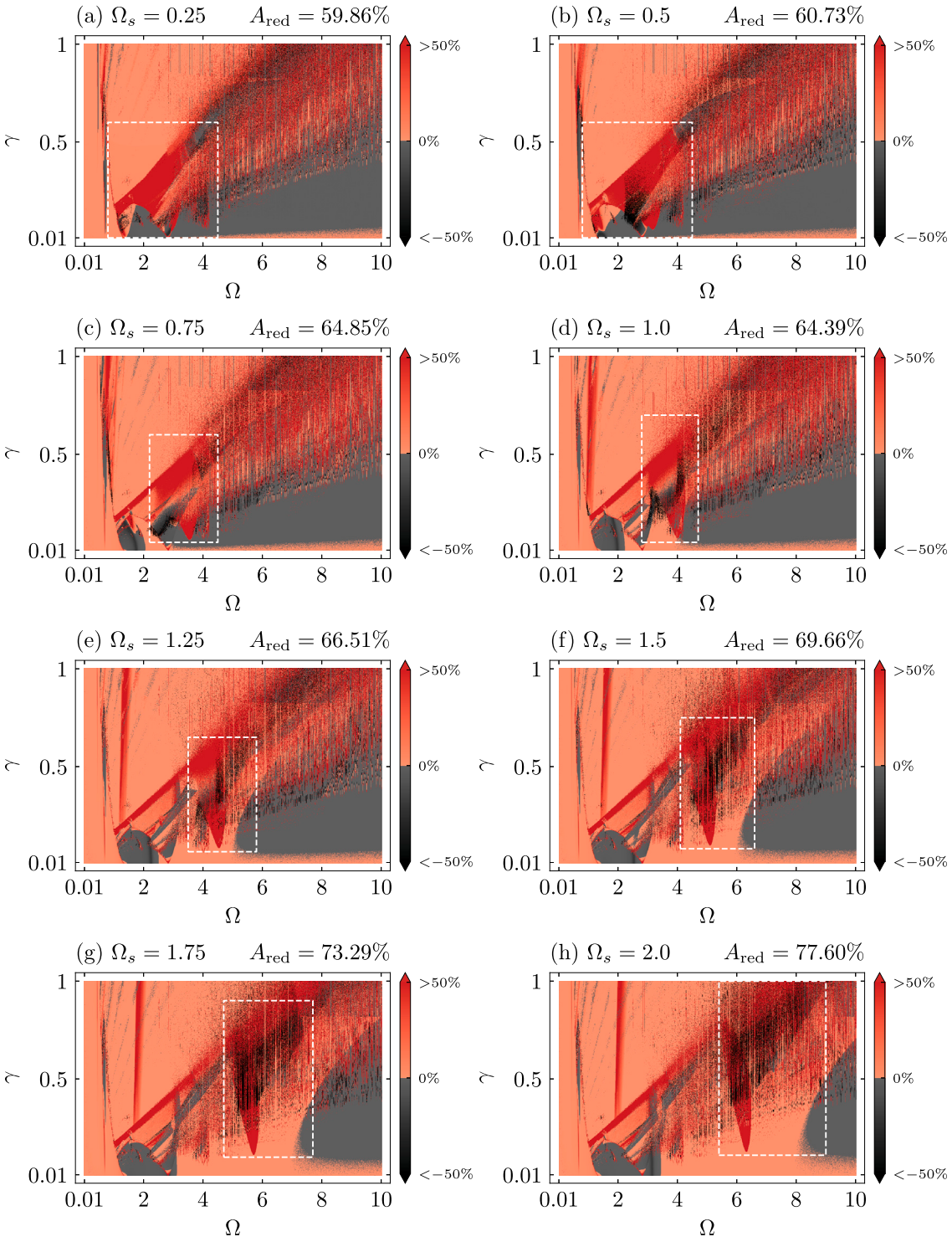

Fig. 17. Comparison of the performance of a multistable 2-degrees-of-freedom energy harvester with a classical bistable energy harvester for different values of Ω_s: (a) $\Omega_s = 0.25$, (b) $\Omega_s = 0.5$, (c) $\Omega_s = 0.75$, (d) $\Omega_s = 1.0$, (e) $\Omega_s = 1.25$, (f) $\Omega_s = 1.5$, (g) $\Omega_s = 1.75$, (h) $\Omega_s = 2.0$. The colorbars represent the percentage difference of average output power, $\Delta\bar{P}_{\text{avg}}(\%)$. The regions in red represent where the multistable 2DoF energy harvester outperforms the classical bistable energy harvester, while black regions show where the classical bistable energy harvester performs better. The performance comparison is done using Eq. (17). Moreover, the white dashed rectangles represent regions of interest discussed in the text.

device with $\Omega_s = 0.25$ and its counterparts with increasing values of Ω_s. Black regions depict where the multistable 2-DoF harvester with $\Omega_s = 0.25$ outperform its counterparts, while red regions where it underperforms. It is noteworthy that the increase of Ω_s promotes enhanced performance at higher frequencies as depicted by the performance comparison diagrams (PCDs). As expected, the difference in performance between the compared harvesters increases in regions where each one performs better.

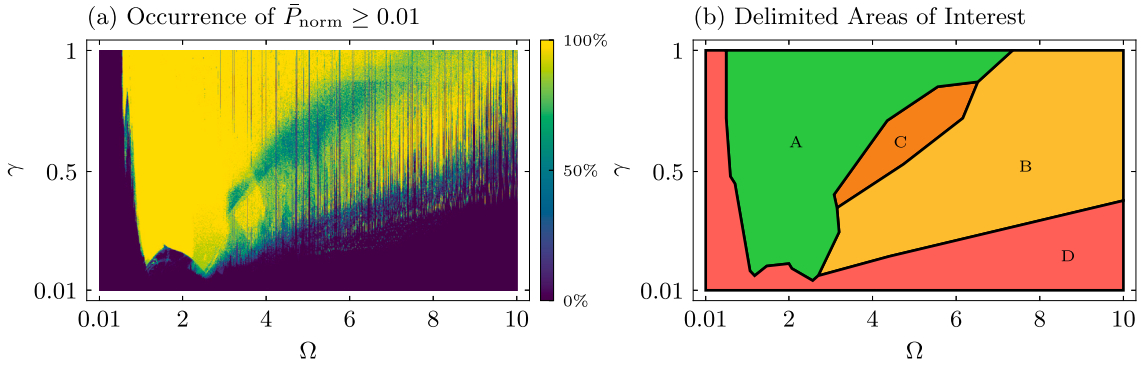

Fig. 18. (a) Occurrence of $\bar{P}_{\text{norm}} \geq 0.01$. (b) identified regions of interest. The colorbar in (a) represent the occurrence in percentage form. The labels A, B, C and D represent each colored region, being A the region of best performance, B and C the regions of moderate performance, and D the region of poor performance in the $\gamma \times \Omega$ parameter domain.

5. Conclusions

In this work, a new compact mechanical energy harvester is presented, aiming applications with limited available spaces, while maintaining optimal performance. A multistable nonlinear structure is designed by incorporating key features of the classical bistable energy harvester and the bistable dual inner-outer beam structure previously described in the literature.

The proposed system integrates the compact arrangement of the dual beams, enhanced by magnetic interactions provided by two sets of magnets and transducers. These magnetic interactions provide unprecedented multistable characteristics to the system, and the usage of two transducers enables the advantageous utilization of free useful space within the structure to enhance energy harvesting capacity.

Nonlinear dynamics perspective is adopted to establish a standardized analysis framework of multistable systems, employing suitable tools and methods. A 2-DoF electromechanical reduced-order model is developed, representing the main qualitative aspects of the proposed energy harvester. Magnetic interactions are modeled by Duffing-type terms, and the model is normalized to isolate key relationships between system parameters.

Stability analysis reveals that the system can exhibit up to 9 equilibrium points, with 4 stable and 5 unstable points. However, by increasing the stiffness ratio between beams or/and the mass ratio between degrees-of-freedom reduces the number of equilibrium points to 3, with 2 stable and 1 unstable point, at different rates. Based on the stability analysis, two configurations are selected for further dynamical and performance investigations: one with a softer inner beam, which characterizes a multistable state with 4 equilibrium points; and another with the outer and the inner beams with the same stiffness, characterizing a bistable state.

The dynamics of the two configurations are mapped within the external excitation parameter domain, showing rich and complex phenomena characterized by various periodic, chaotic and hyperchaotic orbits. The multistable configuration predominantly exhibits period-1T, period-3T and hyperchaotic orbits, while the bistable configuration additionally shows the emergence of chaotic regions. In both cases, period-2T relevant orbits also arises, but in smaller regions. Other types of dynamical responses are also found but not expressively.

The performance analysis revealed that the output electrical response of the first piezoelectric element is proportional to the displacement of the first degree of freedom, while the response of the second piezoelectric element is proportional to the relative displacement between the first and second degrees of freedom. Furthermore, it is observed that the harvester can display high output power when the system's deflection is sufficient to pass through or around all equilibrium points.

By analyzing additional configurations with different stiffness ratios, it is observed that for multistable configurations with 4 stable positions, period-3T orbits are associated with the majority of the points of maximum output power within the excitation parameter domain. In contrast, bistable configurations exhibit a wider range of dynamical responses (primarily period-1T, period-3T, chaotic and hyperchaotic orbits) for the major proportion of points of maximum output power. Additionally, an increase of performance at higher frequencies is observed as the stiffness ratio increases.

Moreover, regions of interest within the parameter domain are identified based on energy harvesting performance. A comparison between eight different configurations of proposed harvester and the classical bistable harvester is conducted. The proposed harvester exhibits comparable bandwidth to the classical bistable harvester, while surpassing it in terms of output power in almost all operation scenarios of interest. Nevertheless, when considering the output power density, the superiority of the proposed harvester diminishes for specific operational conditions such as moderate performance regions, expressive multiple solution regions, and higher frequencies.

In conclusion, the qualitative analysis presented in this work suggests that the proposed harvester is a promising alternative for applications in closed compact spaces, offering significant advantages over the classical bistable energy harvester. For future works, experimental verification and further model improvements are being pursued to enhance robustness. These next steps can provide verification and strengthen the findings presented in this study, contributing to the strategies to enhance energy harvesting capacity.

CRediT authorship contribution statement

Luã G. Costa: Conceptualization, Methodology, Software, Validation, Formal analysis, Investigation, Writing. **Marcelo A. Savi:** Conceptualization, Methodology, Software, Validation, Formal analysis, Investigation, Writing, Supervision, Writing – reviewing.

Declaration of competing interest

The authors declare that they have no known competing financial interests or personal relationships that could have appeared to influence the work reported in this paper.

Data availability

Data will be made available on request.

Acknowledgments

The authors would like to acknowledge the support of the Brazilian Research Agencies CNPq, CAPES and FAPERJ, Brazil. Also, this research was developed with the support of the Advanced High Performance Computing Nucleus (NACAD) of COPPE at the Federal University of Rio de Janeiro (UFRJ), Brazil.

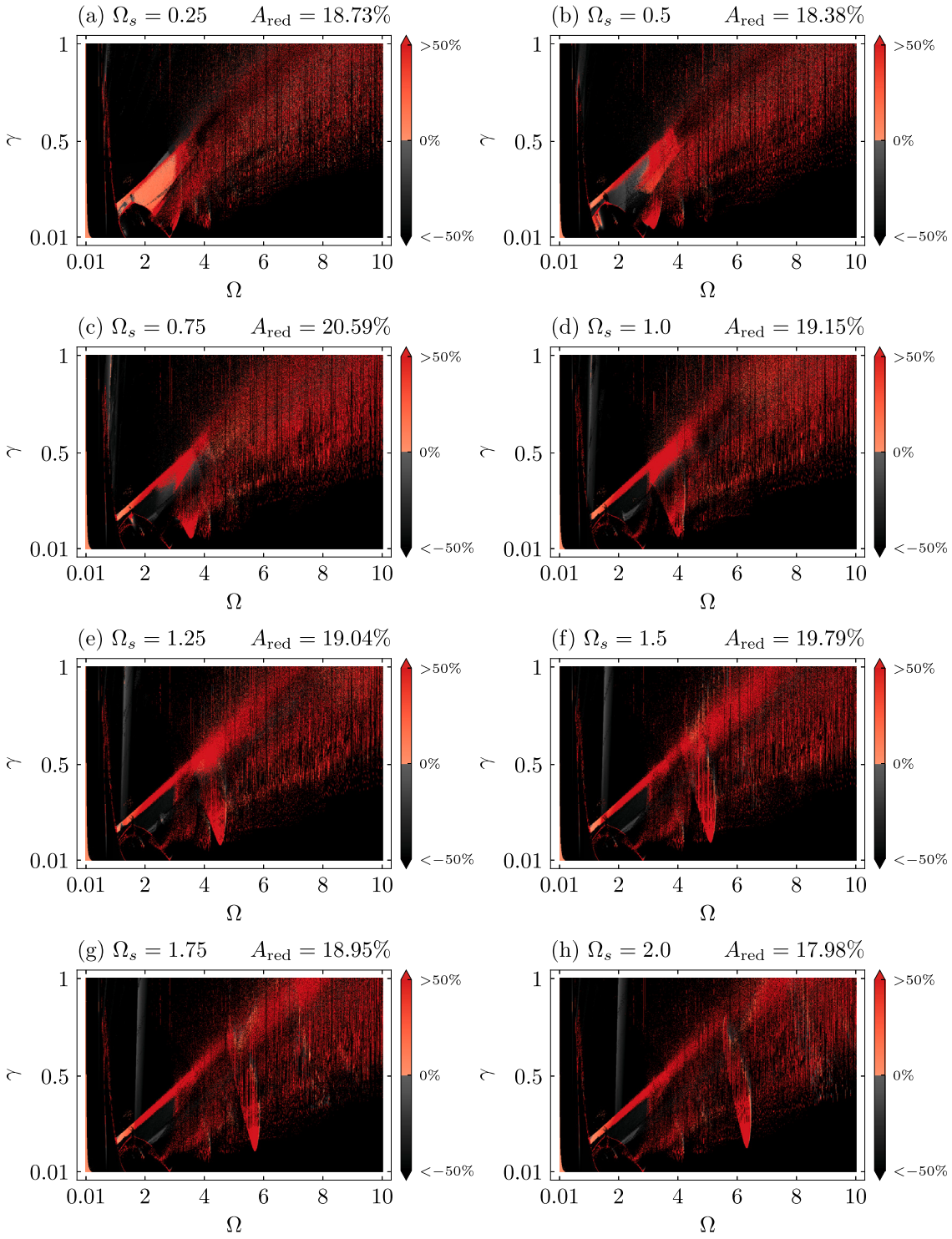

Fig. 19. Comparison of the average output power density $\bar{P}_{\text{avg}}^{\text{den}}$ of a multistable 2-degrees-of-freedom energy harvester with a classical bistable energy harvester for different values of Ω_s: (a) $\Omega_s = 0.25$, (b) $\Omega_s = 0.5$, (c) $\Omega_s = 0.75$, (d) $\Omega_s = 1.0$, (e) $\Omega_s = 1.25$, (f) $\Omega_s = 1.5$, (g) $\Omega_s = 1.75$, (h) $\Omega_s = 2.0$. The colorbars represent the percentage difference of average output power, $\Delta\bar{P}_{\text{avg}}(\%)$. The regions in red represent where the multistable 2DoF energy harvester outperforms the classical bistable energy harvester, while black regions show where the classical bistable energy harvester performs better. The performance comparison is done using Eq. (17).

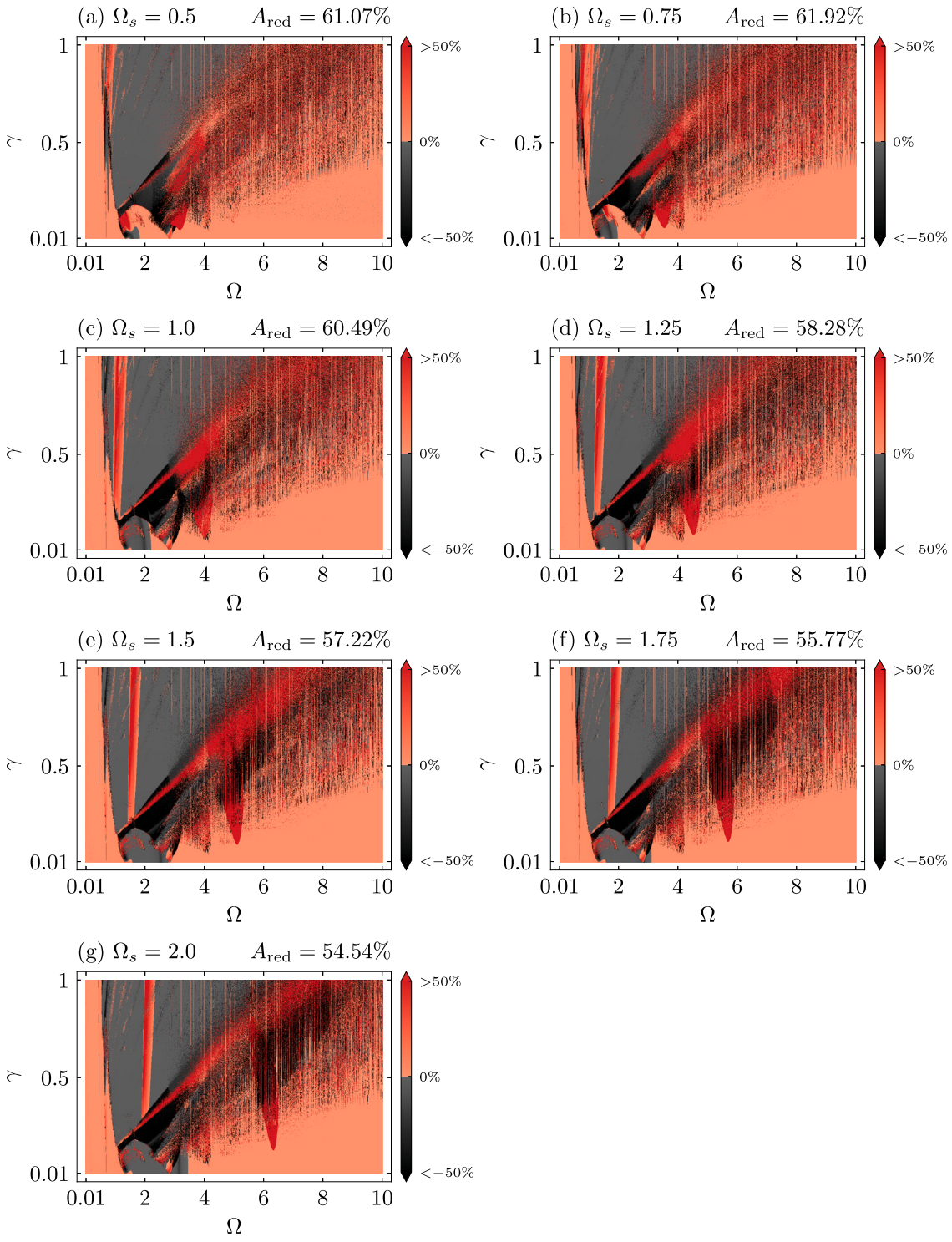

Fig. 20. Comparison of the average output power $\bar{P}_{\text{avg}}$ of a multistable 2-degrees-of-freedom energy harvester in the case of $\Omega = 0.25$ with multistable 2DoF energy harvesters having different values of Ω_s: (a) $\Omega_s = 0.5$, (b) $\Omega_s = 0.75$, (c) $\Omega_s = 1.0$, (d) $\Omega_s = 1.25$, (e) $\Omega_s = 1.5$, (f) $\Omega_s = 1.75$, (g) $\Omega_s = 2.0$. The colorbars represent the percentage difference of average output power, $\Delta\bar{P}_{\text{avg}}(\%)$. The black regions indicate where the multistable 2DoF energy harvester with $\Omega_s = 0.25$ outperforms its counterparts, while red regions show where the multistable 2DoF energy harvester with $\Omega_s = 0.25$ underperforms. The performance comparison is carried out using Eq. (17) modified with the base of comparison being the $\Omega_s = 0.25$ harvester, instead of the CBH.

References

[1] Bose BK. Global warming: Energy, environmental pollution, and the impact of power electronics. IEEE Ind Electron Mag 2010;4(1):6–17. http://dx.doi.org/10.1109/MIE.2010.935860.

[2] Viola FM, Paiva SL, Savi MA. Analysis of the global warming dynamics from temperature time series. Ecol Model 2010;221(16):1964–78. http://dx.doi.org/10.1016/j.ecolmodel.2010.05.001.

[3] Zhu J, Liu X, Shi Q, He T, Sun Z, Guo X, et al. Development trends and perspectives of future sensors and MEMS/NEMS. Micromachines 2020;11(1). http://dx.doi.org/10.3390/mi11010007.

[4] Daqaq MF, Crespo RS, Ha S. On the efficacy of charging a battery using a chaotic energy harvester. Nonlinear Dynam 2020;99(2):1525–37. http://dx.doi.org/10.1007/s11071-019-05372-0.

[5] Toprak A, Tigli O. Piezoelectric energy harvesting: State-of-the-art and challenges. Appl Phys Rev 2014;1(3):031104. http://dx.doi.org/10.1063/1.4896166.
[6] Safaei M, Sodano HA, Anton SR. A review of energy harvesting using piezoelectric materials: State-of-the-art a decade later (2008–2018). Smart Mater Struct 2019;28(11):113001. http://dx.doi.org/10.1088/1361-665X/ab36e4.
[7] Delgado-Alvarado E, Elvira-Hernández EA, Hernández-Hernández J, Huerta-Chua J, Vázquez-Leal H, Martínez-Castillo J, et al. Recent progress of nanogenerators for green energy harvesting: Performance, applications, and challenges. Nanomaterials 2022;12(15). http://dx.doi.org/10.3390/nano12152549.
[8] Liu L, Guo X, Liu W, Lee C. Recent progress in the energy harvesting technology—From self-powered sensors to self-sustained IoT, and new applications. Nanomaterials 2021;11(11). http://dx.doi.org/10.3390/nano11112975.
[9] Deng Z, Dapino MJ. Review of magnetostrictive vibration energy harvesters. Smart Mater Struct 2017;26(10):103001. http://dx.doi.org/10.1088/1361-665X/aa8347.
[10] Narita F, Fox M. A review on piezoelectric, magnetostrictive, and magnetoelectric materials and device technologies for energy harvesting applications. Adv Energy Mater 2018;20(5):1700743. http://dx.doi.org/10.1002/adem.201700743.
[11] Deng Q, Kammoun M, Erturk A, Sharma P. Nanoscale flexoelectric energy harvesting. Int J Solids Struct 2014;51(18):3218–25. http://dx.doi.org/10.1016/j.ijsolstr.2014.05.018.
[12] Tripathy A, Saravanakumar B, Mohanty S, Nayak SK, Ramadoss A. Comprehensive review on flexoelectric energy harvesting technology: Mechanisms, device configurations, and potential applications. ACS Appl Electron Mater 2021;3(7):2898–924. http://dx.doi.org/10.1021/acsaelm.1c00267.
[13] Karaman I, Basaran B, Karaca HE, Karsilayan AI, Chumlyakov YI. Energy harvesting using martensite variant reorientation mechanism in a NiMnGa magnetic shape memory alloy. Appl Phys Lett 2007;90(17):172505. http://dx.doi.org/10.1063/1.2721143.
[14] Rashidi S, Ehsani MH, Shakouri M, Karimi N. Potentials of magnetic shape memory alloys for energy harvesting. J Magn Magn Mater 2021;537:168112. http://dx.doi.org/10.1016/j.jmmm.2021.168112.
[15] Kim D, Hong S, Li D, Roh HS, Ahn G, Kim J, et al. A spring-type piezoelectric energy harvester. RSC Adv 2013;3:3194–8. http://dx.doi.org/10.1039/C2RA22554A.
[16] Kim D, Roh HS, Kim Y, No K, Hong S. Selective current collecting design for spring-type energy harvesters. RSC Adv 2015;5:10662–6. http://dx.doi.org/10.1039/C4RA16443A.
[17] Wang L, Yuan FG. Vibration energy harvesting by magnetostrictive material. Smart Mater Struct 2008;17(4):045009. http://dx.doi.org/10.1088/0964-1726/17/4/045009.
[18] Vallem V, Sargolzaeiaval Y, Ozturk M, Lai Y-C, Dickey MD. Energy harvesting and storage with soft and stretchable materials. Adv Mater 2021;33(19):2004832. http://dx.doi.org/10.1002/adma.202004832.
[19] Erturk A, Tarazaga PA, Farmer JR, Inman DJ. Effect of strain nodes and electrode configuration on piezoelectric energy harvesting from cantilevered beams. J Vib Acoust 2009;131(1). http://dx.doi.org/10.1115/1.2981094, 011010.
[20] Erturk A, Inman DJ. An experimentally validated bimorph cantilever model for piezoelectric energy harvesting from base excitations. Smart Mater Struct 2009;18(2):025009. http://dx.doi.org/10.1088/0964-1726/18/2/025009.
[21] Kim M, Hoegen M, Dugundji J, Wardle BL. Modeling and experimental verification of proof mass effects on vibration energy harvester performance. Smart Mater Struct 2010;19(4):045023. http://dx.doi.org/10.1088/0964-1726/19/4/045023.
[22] Kim JE, Kim YY. Analysis of piezoelectric energy harvesters of a moderate aspect ratio with a distributed tip mass. J Vib Acoust 2011;133(4). http://dx.doi.org/10.1115/1.4003598, 041010.
[23] Zhang H, Corr LR, Ma T. Issues in vibration energy harvesting. J Sound Vib 2018;421:79–90. http://dx.doi.org/10.1016/j.jsv.2018.01.057.
[24] Ou Q, Chen X, Gutschmidt S, Wood A, Leigh N, Arrieta AF. An experimentally validated double-mass piezoelectric cantilever model for broadband vibration–based energy harvesting. J Intell Mater Syst Struct 2012;23(2):117–26. http://dx.doi.org/10.1177/1045389X11431746.
[25] Wu H, Tang L, Yang Y, Soh CK. A novel two-degrees-of-freedom piezoelectric energy harvester. J Intell Mater Syst Struct 2013;24(3):357–68. http://dx.doi.org/10.1177/1045389X12457254.
[26] Zou H-X, Zhao L-C, Gao Q-H, Zuo L, Liu F-R, Tan T, et al. Mechanical modulations for enhancing energy harvesting: Principles, methods and applications. Appl Energy 2019;255:113871. http://dx.doi.org/10.1016/j.apenergy.2019.113871.
[27] Wang T. Pendulum-based vibration energy harvesting: Mechanisms, transducer integration, and applications. Energy Convers Manage 2023;276:116469. http://dx.doi.org/10.1016/j.enconman.2022.116469.
[28] Stanton SC, McGehee CC, Mann BP. Nonlinear dynamics for broadband energy harvesting: Investigation of a bistable piezoelectric inertial generator. Physica D 2010;239(10):640–53. http://dx.doi.org/10.1016/j.physd.2010.01.019.
[29] Osinaga S, Machado S, Febbo M. An analytical model of the electromechanical coupling for a piezoelectric stepped buckled beam for energy harvesting applications. Mech Syst Signal Process 2022;179:109355. http://dx.doi.org/10.1016/j.ymssp.2022.109355.
[30] Zhu Y, Zu JW. Enhanced buckled-beam piezoelectric energy harvesting using midpoint magnetic force. Appl Phys Lett 2013;103(4):041905. http://dx.doi.org/10.1063/1.4816518.
[31] Costa LG, da Silva Monteiro LL, Pacheco PMCL, Savi MA. A parametric analysis of the nonlinear dynamics of bistable vibration-based piezoelectric energy harvesters. J Intell Mater Syst Struct 2021;32(7):699–723. http://dx.doi.org/10.1177/1045389X20963188.
[32] Masana R, Daqaq MF. Electromechanical modeling and nonlinear analysis of axially loaded energy harvesters. J Vib Acoust 2010;133(1). http://dx.doi.org/10.1115/1.4002786, 011007.
[33] Kumar KA, Ali SF, Arockiarajan A. Piezomagnetoelastic broadband energy harvester: Nonlinear modeling and characterization. Eur Phys J Spec Top 2015/11/01;224(14):2803–22. http://dx.doi.org/10.1140/epjst/e2015-02590-8.
[34] Panyam M, Daqaq MF. Characterizing the effective bandwidth of tri-stable energy harvesters. J Sound Vib 2017;386:336–58. http://dx.doi.org/10.1016/j.jsv.2016.09.022.
[35] Zhou Z, Qin W, Zhu P. A broadband quad-stable energy harvester and its advantages over bi-stable harvester: Simulation and experiment verification. Mech Syst Signal Process 2017;84:158–68. http://dx.doi.org/10.1016/j.ymssp.2016.07.001.
[36] Sun S, Leng Y, Hur S, Sun F, Su X, Song H-C, et al. Energy harvesting performance of a novel nonlinear quad-stable piezoelectric energy harvester with only one external magnet. Machines 2022;10(9). http://dx.doi.org/10.3390/machines10090803.
[37] Zhou Z, Qin W, Yang Y, Zhu P. Improving efficiency of energy harvesting by a novel penta-stable configuration. Sensors Actuators A 2017;265:297–305. http://dx.doi.org/10.1016/j.sna.2017.08.039.
[38] Lallart M, Zhou S, Yan L, Yang Z, Chen Y. Tailoring multistable vibrational energy harvesters for enhanced performance: Theory and numerical investigation. Nonlinear Dynam 2019;96(2):1283–301. http://dx.doi.org/10.1007/s11071-019-04853-6.
[39] Kumar A, Ali SF, Arockiarajan A. Exploring the benefits of an asymmetric monostable potential function in broadband vibration energy harvesting. Appl Phys Lett 2018;112(23):233901. http://dx.doi.org/10.1063/1.5037733.
[40] Wang W, Cao J, Bowen CR, Litak G. Multiple solutions of asymmetric potential bistable energy harvesters: numerical simulation and experimental validation. Eur Phys J B 2018;91(10):254. http://dx.doi.org/10.1140/epjb/e2018-90180-y.
[41] Cao J, Zhou S, Inman DJ, Lin J. Nonlinear dynamic characteristics of variable inclination magnetically coupled piezoelectric energy harvesters. J Vib Acoust 2015;137(2):021015. http://dx.doi.org/10.1115/1.4029076.
[42] Norenberg JP, Luo R, Lopes VG, Peterson JVL, Cunha A. Nonlinear dynamics of asymmetric bistable energy harvesters. Int J Mech Sci 2023;257:108542. http://dx.doi.org/10.1016/j.ijmecsci.2023.108542.
[43] Ai R, Monteiro LLS, Monteiro PCC, Pacheco PMCL, Savi MA. Piezoelectric vibration-based energy harvesting enhancement exploiting nonsmoothness. Actuators 2019;8(1). http://dx.doi.org/10.3390/act8010025.
[44] Ahmad MM, Khan NM, Khan FU. Review of frequency up-conversion vibration energy harvesters using impact and plucking mechanism. Int J Energy Res 2021;45(11):15609–45. http://dx.doi.org/10.1002/er.6832.
[45] Adeodato A, Duarte BT, Monteiro LLS, Pacheco PMC, Savi MA. Synergistic use of piezoelectric and shape memory alloy elements for vibration-based energy harvesting. Int J Mech Sci 2021;194:106206. http://dx.doi.org/10.1016/j.ijmecsci.2020.106206.
[46] Yuan JH, Yang YZ, Zhang YH. A piezoelectric energy harvester with light-activated shape memory polymers. Ferroelectrics 2019;550(1):98–111. http://dx.doi.org/10.1080/00150193.2019.1652500.
[47] Margielewicz J, Gaska D, Litak G, Wolszczak P, Yurchenko D. Nonlinear dynamics of a new energy harvesting system with quasi-zero stiffness. Appl Energy 2022;307:118159. http://dx.doi.org/10.1016/j.apenergy.2021.118159.
[48] Caetano VJ, Savi MA. Multimodal pizza-shaped piezoelectric vibration-based energy harvesters. J Intell Mater Syst Struct 2021;32(20):2505–28. http://dx.doi.org/10.1177/1045389X211006910.
[49] Caetano VJ, Savi MA. Star-shaped piezoelectric mechanical energy harvesters for multidirectional sources. Int J Mech Sci 2022;215:106962. http://dx.doi.org/10.1016/j.ijmecsci.2021.106962.
[50] Yang Z, Wang YQ, Zuo L, Zu J. Introducing arc-shaped piezoelectric elements into energy harvesters. Energy Convers Manage 2017;148:260–6. http://dx.doi.org/10.1016/j.enconman.2017.05.073.
[51] Zhou W, Wang B, Lim C, Yang Z. A distributed-parameter electromechanical coupling model for a segmented arc-shaped piezoelectric energy harvester. Mech Syst Signal Process 2021;146:107005. http://dx.doi.org/10.1016/j.ymssp.2020.107005.
[52] Chen X, Zhang X, Wang L, Chen L. An arch-linear composed beam piezoelectric energy harvester with magnetic coupling: Design, modeling and dynamic analysis. J Sound Vib 2021;513:116394. http://dx.doi.org/10.1016/j.jsv.2021.116394.
[53] Zhang X, Yang W, Zuo M, Tan H, Fan H, Mao Q, et al. An arc-shaped piezoelectric bistable vibration energy harvester: Modeling and experiments. Sensors 2018;18(12). http://dx.doi.org/10.3390/s18124472.

[54] Zhang X, Zuo M, Yang W, Wan X. A tri-stable piezoelectric vibration energy harvester for composite shape beam: Nonlinear modeling and analysis. Sensors 2020;20(5). http://dx.doi.org/10.3390/s20051370.

[55] Chen X, Zhang X, Chen L, Guo Y, Zhu F. A curve-shaped beam bistable piezoelectric energy harvester with variable potential well: Modeling and numerical simulation. Micromachines 2021;12(8). http://dx.doi.org/10.3390/mi12080995.

[56] Wu Y, Qiu J, Zhou S, Ji H, Chen Y, Li S. A piezoelectric spring pendulum oscillator used for multi-directional and ultra-low frequency vibration energy harvesting. Appl Energy 2018;231:600–14. http://dx.doi.org/10.1016/j.apenergy.2018.09.082.

[57] Fu H, Yeatman EM. A methodology for low-speed broadband rotational energy harvesting using piezoelectric transduction and frequency up-conversion. Energy 2017;125:152–61. http://dx.doi.org/10.1016/j.energy.2017.02.115.

[58] Fu H, Jiang J, Hu S, Rao J, Theodossiades S. A multi-stable ultra-low frequency energy harvester using a nonlinear pendulum and piezoelectric transduction for self-powered sensing. Mech Syst Signal Process 2023;189:110034. http://dx.doi.org/10.1016/j.ymssp.2022.110034.

[59] Mei X, Zhou S, Yang Z, Kaizuka T, Nakano K. Enhancing energy harvesting in low-frequency rotational motion by a quad-stable energy harvester with time-varying potential wells. Mech Syst Signal Process 2021;148:107167. http://dx.doi.org/10.1016/j.ymssp.2020.107167.

[60] Hu G, Tang L, Das R. Internally coupled metamaterial beam for simultaneous vibration suppression and low frequency energy harvesting. J Appl Phys 2018;123(5):055107. http://dx.doi.org/10.1063/1.5011999.

[61] Akaydın HD, Elvin N, Andreopoulos Y. Wake of a cylinder: A paradigm for energy harvesting with piezoelectric materials. Exp Fluids 2010;49(1):291–304. http://dx.doi.org/10.1007/s00348-010-0871-7.

[62] Tandel R, Shah S, Tripathi S. A state-of-art review on bladeless wind turbine. J Phys Conf Ser 2021;1950(1):012058. http://dx.doi.org/10.1088/1742-6596/1950/1/012058.

[63] Wang J, Zhou S, Zhang Z, Yurchenko D. High-performance piezoelectric wind energy harvester with Y-shaped attachments. Energy Convers Manage 2019;181:645–52. http://dx.doi.org/10.1016/j.enconman.2018.12.034.

[64] Wu H, Tang L, Yang Y, Soh CK. Development of a broadband nonlinear two-degree-of-freedom piezoelectric energy harvester. J Intell Mater Syst Struct 2014;25(14):1875–89. http://dx.doi.org/10.1177/1045389X14541494.

[65] Upadrashta D, Yang Y. Finite element modeling of nonlinear piezoelectric energy harvesters with magnetic interaction. Smart Mater Struct 2015;24(4):045042. http://dx.doi.org/10.1088/0964-1726/24/4/045042.

[66] Krishnasamy M, Upadrashta D, Yang Y, Lenka TR. Distributed parameter modelling of cutout 2-DOF cantilevered piezo-magneto-elastic energy harvester. J Microelectromech Syst 2018;27(6):1160–70. http://dx.doi.org/10.1109/JMEMS.2018.2875788.

[67] Zhao L, Tang L, Yang Y. Enhanced piezoelectric galloping energy harvesting using 2 degree-of-freedom cut-out cantilever with magnetic interaction. Japan J Appl Phys 2014;53(6):060302. http://dx.doi.org/10.7567/JJAP.53.060302.

[68] Bouhedma S, Zheng Y, Lange F, Hohlfeld D. Magnetic frequency tuning of a multimodal vibration energy harvester. Sensors 2019;19(5). http://dx.doi.org/10.3390/s19051149.

[69] Erturk A, Inman D. Broadband piezoelectric power generation on high-energy orbits of the bistable duffing oscillator with electromechanical coupling. J Sound Vib 2011;330(10):2339–53. http://dx.doi.org/10.1016/j.jsv.2010.11.018, Dynamics of Vibro-Impact Systems.

[70] De Paula AS, Inman DJ, Savi MA. Energy harvesting in a nonlinear piezo-magnetoelastic beam subjected to random excitation. Mech Syst Signal Process 2015;54–55:405–16. http://dx.doi.org/10.1016/j.ymssp.2014.08.020.

[71] Rezaei M, Talebitooti R, Liao W-H. Exploiting bi-stable magneto-piezoelastic absorber for simultaneous energy harvesting and vibration mitigation. Int J Mech Sci 2021;207:106618. http://dx.doi.org/10.1016/j.ijmecsci.2021.106618.

[72] Preumont A. Mechatronics: dynamics of electromechanical and piezoelectric systems. Dordrecht: Springer Netherlands; 2006, http://dx.doi.org/10.1007/1-4020-4696-0.

[73] Meirovitch L. Methods of analytical dynamics. Advanced engineering series, Dover Publications; 2010.

[74] Savi MA. Nonlinear dynamics and chaos. In: Lopes Jr. V, Steffen Jr. V, Savi MA, editors. Dynamics of smart systems and structures: concepts and applications. Cham: Springer International Publishing; 2016, p. 93–117. http://dx.doi.org/10.1007/978-3-319-29982-2_5.

[75] Wolf A, Swift JB, Swinney HL, Vastano JA. Determining Lyapunov exponents from a time series. Physica D 1985;16(3):285–317. http://dx.doi.org/10.1016/0167-2789(85)90011-9.